

The following publication Kang, F., Sun, G., Wang, A., Xiao, X., Li, Y. Y., Lu, J., & Huang, B. (2018). Multicolor tuning and temperature-triggered anomalous Eu<sup>3+</sup>-related photoemission enhancement via interplay of accelerated energy transfer and release of defect-trapped electrons in the Tb<sup>3+</sup>, Eu<sup>3+</sup>-doped strontium–aluminum chlorites. *ACS applied materials & interfaces*, 10(42), 36157-36170 is available at <https://doi.org/10.1021/acsami.8b13728>.

## Multicolor Tuning and Temperature-Triggered Anomalous Eu<sup>3+</sup>-related Photoemission Enhancement via Interplay of Accelerated Energy Transfer and Release of Defect-Trapped Electrons in the Tb<sup>3+</sup>, Eu<sup>3+</sup> doped Strontium-Aluminum Chlorites

Fengwen Kang,<sup>a,b</sup> Guohuan Sun,<sup>c</sup> Yangyang Li,<sup>\*b</sup> Jian Lu,<sup>\*b</sup> and Bolong Huang,<sup>\*d</sup>

<sup>a</sup>The State Key Laboratory of Luminescent Materials and Devices, Guangdong Provincial Key Laboratory of Fiber Laser Materials and Applied Techniques, Guangdong Engineering Technology Research and Development Center of Special Optical Fiber Materials and Devices, School of Materials Science and Technology, South China University of Technology, Guangzhou 510640, P. R. China; <sup>b</sup>Department of Mechanical and Biomedical Engineering (MBE), City University of Hong Kong, Hong Kong, China; <sup>c</sup>the State Key Laboratory of Experimental Hematology, SKLEH, Institute of Hematology, Chinese Academy of Medical Sciences, Tianjin 300020, P.R. China; <sup>d</sup>Department of Applied Biology and Chemical Technology, The Hong Kong Polytechnic University, Hung Hom, Kowloon, Hong Kong SAR; <sup>e</sup> Department of Applied Physics, The Hong Kong Polytechnic University, Hong Kong, China.

### Abstract

So far, a large number of rare earth (RE) and non-RE doped emission-tunable crystals based on controllable energy transfer have become available, but numerous mechanistic issues, particularly for those that involve temperature-dependent energy transfer interaction between the well-shielded 4f RE ions, lack comprehensive theoretical and experimental investigation, which limit greatly the development of their new applications. Here, we design and report a type of Tb<sup>3+</sup>, Eu<sup>3+</sup> doped Sr<sub>3</sub>Al<sub>2</sub>O<sub>5</sub>Cl<sub>2</sub> phosphors capable of multi emissions upon excitation at 376 nm, through using the orthorhombic Sr<sub>3</sub>Al<sub>2</sub>O<sub>5</sub>Cl<sub>2</sub> crystal as host lattice while the well-shielded 4f Tb<sup>3+</sup> and Eu<sup>3+</sup> ions as dual luminescent centers. Our results reveal that the energy transfer from Tb<sup>3+</sup> to Eu<sup>3+</sup> ions, which is happened *via* an electric dipole-quadrupole (*d-q*) interaction, can be controlled by the doping ratio of Tb<sup>3+</sup> and Eu<sup>3+</sup>, leading to precisely tunable emissions from green (0.3159, 0.5572) to red (0.6579, 0.3046). It is found from time-resolved photoluminescence (PL) spectra that such energy transfer begins at  $t = 5 \mu\text{s}$  and gradually ends at  $t \geq 200 \mu\text{s}$ . Moreover, from temperature-dependent PL results, we reveal for the first time that the Eu<sup>3+</sup> emission features an anomalous intensity enhancement at the earlier heating state. With the density functional theory (DFT) calculations, we have screened all the possibilities of site occupancy preference and revealed that Eu<sup>3+</sup> and Tb<sup>3+</sup> tend to substitute Sr<sup>2+</sup> and Al<sup>3+</sup>, respectively. By jointly taking into account the XRD Rietveld refinement, DFT findings, PL and thermoluminescence (TL) spectra, a mechanistic profile is proposed for illustrating the observed color tuning and temperature-triggered anomalous Eu<sup>3+</sup> emission enhancement. In particular, our discussions reveal that the latter is due to the interplay of the temperature-induced accelerated energy transfer and defect-trapped electrons that are released upon thermal stimulation. Unlike most of reported phosphor materials that are always suggested for wLEDs, we also demonstrate new possibilities for Tb<sup>3+</sup>, Eu<sup>3+</sup> doped Sr<sub>3</sub>Al<sub>2</sub>O<sub>5</sub>Cl<sub>2</sub> phosphors for temperature-controlled fluorescence sensor, anti-counterfeiting, data storage and security devices.

### \*Corresponding authors

Email: [yangli@cityu.edu.hk](mailto:yangli@cityu.edu.hk); [jianlu@cityu.edu.hk](mailto:jianlu@cityu.edu.hk); and [bhuang@polyu.edu.hk](mailto:bhuang@polyu.edu.hk)

## 1. INTRODUCTION

Due to the plentiful spectral properties, the phosphor materials have been intensively suggested for wide-ranging applications, such as phosphor-converted white light-emitting diodes (pc-wLEDs) [1-2], photocatalysts [3-5], agricultural promotion for plant growth [6-7], biomedical imaging and illumination [8-9]. In general, desired emission properties are mainly achieved through mixing multiple phosphors of different colors. However, such approach frequently suffers from visible re-absorption, complicated device design, color imbalance and instability resulted from different responses of multiple phosphors to environmental factors, *e.g.*, temperature of the LED chip. In comparison, single-phased tunable phosphors enable desirable wavelength conveniently without worrying about the above problems, attracting tremendous research interest which leads to a variety of tuning strategies through modulation of excitation wavelength [11-13], energy transfer [11, 14-17], crystal field [14, 18-19], electronic band-gap [20], site occupation preference [21-22], cation nanosegregation [23], chemical unit cosubstitution [24], and temperature [25-27]. Among them, the most common method is the energy transfer control between different activators, which has been demonstrated to exhibit plentiful emissions across a broad range of visible spectra in different systems, such as,  $\text{Ca}_5(\text{PO}_4)_3\text{Cl}:\text{Ce}^{3+}/\text{Eu}^{2+}, \text{Tb}^{3+}/\text{Mn}^{2+}$  (blue  $\rightarrow$  green  $\rightarrow$  white) [21],  $\text{Sr}_3\text{Y}_2(\text{Si}_3\text{O}_9)_2:\text{Ce}^{3+}, \text{Tb}^{3+}/\text{Mn}^{2+}/\text{Eu}^{2+}$  (blue  $\rightarrow$  green  $\rightarrow$  green) [28],  $(\text{Gd-Y-Bi-Eu})\text{VO}_4$  (green  $\rightarrow$  red) [29],  $\text{Ca}_9\text{Mg}(\text{PO}_4)_6\text{F}_2:\text{Eu}^{2+}, \text{Mn}^{2+}$  (blue  $\rightarrow$  yellow) [30]. Nevertheless, the study of above strategies always involves similar and routine PL characterizations such as the XRD, static and dynamic PL spectra as well as a feasible energy transfer profile, being limited to experimental PL observations and mechanistic discussions. And thus, it lacks but remains a big room for in-depth understanding of the energy transfer mechanism. Moreover, it should be pointed out that the RE and non-RE ions commonly used in the energy transfer that possess *f-d* (*e.g.*,  $\text{Dy}^{3+}$ ,  $\text{Eu}^{2+}$ , and  $\text{Ce}^{3+}$ ) and *S-P* (*e.g.*,  $\text{Bi}^{3+}$ ,  $\text{Bi}^{2+}$ ) transitions are hypersensitive to the local environment and their locations in the host lattice, leading to broad excitation and emission bands and thus often severe visible re-absorption and instable emission position and shape during heating treatment. Hence, such RE and non-RE ions actually are undesirable for studying the energy transfer mechanism and the PL properties at high temperature. By contrast, the trivalent RE ions (*e.g.*,  $\text{Sm}^{3+}$ ,  $\text{Pr}^{3+}$ ,  $\text{Tb}^{3+}$ ,  $\text{Eu}^{3+}$ ,  $\text{Tm}^{3+}$ ,  $\text{Yb}^{3+}$ , and  $\text{Er}^{3+}$ ), featuring the well-shielded *4f* electrons configuration and typically *f-f* transition, display much higher stability of spectral positions and shape due to their insensitive to external stimulus

(*e.g.*, temperature change) and the host lattice, which, however, poses a challenge for unveiling their PL mechanism typically when crystals with multi available sites are involved.

Besides, several questions that involve the energy transfer interaction between the well-shielded  $4f$  ions still remain not answered, when this energy transfer interaction starts, weakens and ends; how this interaction behaves with the increase of delay time; how the temperature affects respectively the thermally-induced luminescence quenching of different  $4f$  ions and their interactions; how to understand the unexpected temperature-induced anomalous PL properties and how to utilize their properties to explore new applications rather than the traditional wLED applications. In this case, it would be extremely desirable and also of scientific importance to design a type of phosphor material system that can answer all the above-mentioned issues in the lighting field.

In this study, the  $\text{Sr}_3\text{Al}_2\text{O}_5\text{Cl}_2$ , as one member of orthorhombic-typed family [31-36], is selected and found for the first time to be the desired material system for in-depth understanding of all the above-mentioned questions on the energy transfer interaction between the well-shielded  $4f$  RE ions. Notably, the crystalline  $\text{Sr}_3\text{Al}_2\text{O}_5\text{Cl}_2$  [31-36] has been reported to exhibit the UV-converted afterglow luminescence with trivalent RE ions, such as  $\text{Tb}^{3+}$  [31-32],  $\text{Ce}^{3+}$  [33-36], and  $\text{Pr}^{3+}$  [36]. Tunable emissions have been also realized by doping  $\text{Sr}_3\text{Al}_2\text{O}_5\text{Cl}_2$  with  $\text{Dy}^{3+}/\text{Eu}^{2+}$  [33] and  $\text{Ce}^{3+}/\text{Eu}^{2+}$  [35] as a result of the energy transfer from  $\text{Ce}^{3+}$  to  $\text{Eu}^{2+}$  ion and  $\text{Dy}^{3+}$  to  $\text{Eu}^{2+}$  ion. Other dual-ions doped  $\text{Sr}_3\text{Al}_2\text{O}_5\text{Cl}_2$ , however, is rarely studied. On the other hand, due to the sensitivity of the  $f-d$  transition to its local environment,  $\text{Dy}^{3+}$ ,  $\text{Eu}^{2+}$  and  $\text{Ce}^{3+}$  doped  $\text{Sr}_3\text{Al}_2\text{O}_5\text{Cl}_2$  phosphors exhibit broad excitation and emission bands [33], resulting in the PL quenching, instable spectral positions upon thermal treatment, again confirming the  $f-d$  RE activators is not desirable for studying the energy transfer interaction behavior. As a result, we seek for alternative activators that feature controllable energy transfer and stable PL positions. It is well-known that when  $\text{Tb}^{3+}$  and  $\text{Eu}^{3+}$  ions are simultaneously incorporated into a crystal host (*e.g.*,  $\text{NaLa}(\text{PO}_3)_4$  [37],  $\text{Y}_2\text{SiO}_5$  [38],  $\beta\text{-NaGdF}_4$  [39], and  $\text{Ga}_2\text{O}_3$  [40]), by adjusting the ratio of  $\text{Tb}^{3+}$  and  $\text{Eu}^{3+}$ , the energy transfer from  $\text{Tb}^{3+}$  to  $\text{Eu}^{3+}$  ions and sometimes simultaneous emissions of  $\text{Tb}^{3+}$  and  $\text{Eu}^{3+}$  upon excitation at the wavelength of  $\text{Tb}^{3+}$  can be achieved. Enlightened by this fact,  $\text{Sr}_3\text{Al}_2\text{O}_5\text{Cl}_2:\text{Tb}^{3+},\text{Eu}^{3+}$  phosphor is designed for realization of tunable emissions from green to red. Furthermore, the previously reported  $\text{Sr}_3\text{Al}_2\text{O}_5\text{Cl}_2$  systems were generally investigated at ambient temperature, with no special attention paid to the temperature-dependent PL mechanism. Moreover, the other reason for us to

choose this crystal is based on the consideration that each Sr atom (**Figure 1(a)**) is coordinated with 5 oxygen and 4 chlorine atoms, which can group into three types of  $\text{Sr}^{3+}$  sites (*i.e.*, Sr1, Sr2, and Sr3) based on the different Sr-O and Sr-Cl bond lengths (**Table 1**). All the  $\text{Al}^{3+}$  ions are coordinated with 4 oxygen atoms, forming the  $[\text{AlO}_4]$  tetrahedrons. Both  $\text{SrO}_5\text{Cl}_4$  and  $[\text{AlO}_4]$  structures are connected by the oxygen atoms, without involving the chlorine atoms. Clearly, the unit cell of  $\text{Sr}_3\text{Al}_2\text{O}_5\text{Cl}_2$  has multiple sites for the  $4f$  RE doping, making it an promising host for studying the energy transfer interaction, preferential site substitution, and temperature-dependent PL properties, while capable of triggering some unexpected PL properties and eventually enabling new applications. Specifically,  $\text{Tb}^{3+}$ ,  $\text{Eu}^{3+}$  doped  $\text{Sr}_3\text{Al}_2\text{O}_5\text{Cl}_2$  phosphors, with the  $\text{Sr}_3\text{Al}_2\text{O}_5\text{Cl}_2$  for hosting the well-shielded  $4f$   $\text{Tb}^{3+}$  and  $\text{Eu}^{3+}$  as respective green and red emitting components, are synthesized by the high temperature solid state reactions, and further investigated, particularly for their temperature-dependent PL behaviors. As a consequence, we achieve the tunable colors from green (0.3159, 0.5572) to red (0.6579, 0.3046) by tuning the content ratio of  $\text{Tb}^{3+}$  and  $\text{Eu}^{3+}$ . Furthermore, it is found that the energy transfer from  $\text{Tb}^{3+}$  to  $\text{Eu}^{3+}$  ions, which happened through an electric dipole-quadrupole ( $d-q$ ) interaction, begins at  $t = 5 \mu\text{s}$  and gradually vanishes after  $t \geq 200 \mu\text{s}$ . Interestingly, the  $\text{Sr}_3\text{Al}_2\text{O}_5\text{Cl}_2:\text{Tb}^{3+},\text{Eu}^{3+}$  phosphor exhibit unexpected anomalous  $\text{Eu}^{3+}$ -related photoemission enhancement at the earlier heating state. The DFT modeling indicates that the  $\text{Eu}^{3+}$  and  $\text{Tb}^{3+}$  ions tend to substitute for the  $\text{Sr}^{2+}$  and  $\text{Al}^{3+}$  sites, respectively. Discussions further reveal that the  $\text{Eu}^{3+}$ -related photoemission enhancement is due to the interplay of the temperature-triggered accelerated energy transfer and the release of defect-trapped electrons upon thermal stimulation. Demo applications indicates that the  $\text{Sr}_3\text{Al}_2\text{O}_5\text{Cl}_2:\text{Tb}^{3+},\text{Eu}^{3+}$  phosphor could be suggested for temperature-dependent fluorescence sensor, anti-counterfeiting, data storage and security devices such as emergency signs.

## 2. EXPERIMENTAL AND THEORETICAL DETAILS

### 2.1 Synthesis of samples

Considering the possibility of the future large scale production, the high temperature solid-state reaction method, which has been accepted as one of the most frequently-used methods in commercial production, was used to prepare the phosphors, *i.e.*,  $\text{Sr}_{3-x}\text{Al}_2\text{O}_5\text{Cl}_2:x\text{Tb}^{3+}$  ( $x = 0, 0.25\%, 0.5\%, 0.75\%, 1.0\%, 1.25\%, 1.5\%, 1.75\%, 2.0\%, 2.25\%, 2.5\%, 3.0\%$ ),  $\text{Sr}_{3-y}\text{Al}_2\text{O}_5\text{Cl}_2:y\text{Eu}^{3+}$  ( $y = 0.25\%, 0.5\%, 1.0\%, 1.5\%, 2.0\%, 2.5\%, 3.0\%$ ), and  $\text{Sr}_{3-x-z}\text{Al}_2\text{O}_5\text{Cl}_2:x\text{Tb}^{3+},z\text{Eu}^{3+}$  ( $x = 1.5\%, z =$

0.25%, 0.5%, 0.75%, 1.0%, 1.25%, 1.5%, 1.75%, 2.0%). Specifically, according to the nominal chemical compositions, the as-purchased reagents, SrCl<sub>2</sub>·6H<sub>2</sub>O (A. R., A. R. denotes analytical reagent), Al<sub>2</sub>O<sub>3</sub> (A. R.), Eu<sub>2</sub>O<sub>3</sub> (99.99%), and Tb<sub>2</sub>O<sub>3</sub> (99.99%), were weighed and mixed for 0.5 h in an agate mortar. Then, the powders were transferred to a corundum crucible and pre-sintered at 800 °C for 1 h in air. After grinding the pre-sintered powders for 15 min and sintering at 1200 °C for 4 h in air again, the targeted samples in form of faint yellow were obtained. Previous works indicated that the temperature of 1200 °C was the optimal temperature for accessing the desirable phase-purity of Sr<sub>3</sub>Al<sub>2</sub>O<sub>5</sub>Cl<sub>2</sub> crystal [31, 36] and, thus, was also employed in this work.

**Table 1** Bond length  $d$  (Å) of Sr<sub>2.965</sub>Al<sub>2</sub>O<sub>5</sub>Cl<sub>2</sub> compound, data are from ICSD standard card

Bond type	Bond length $d$ / Å	Bond type	Bond length $d$ / Å
Sr1-O	2.5446	Sr1-Cl	3.0728
	2.5229		3.1297
	2.4331		3.1944
	2.8333		3.3464
	3.3982		---
Sr2-O	2.5269	Sr2-Cl	3.1039
	2.4605		3.1134
	2.4368		3.3820
	3.0476		3.1521
	3.1814		---
Sr3-O	2.4592	Sr3-Cl	3.2786
	2.5197		3.0998
	2.4007		3.0979
	3.1199		3.2547
	3.1107		---

## 2.2 Characterization Details

Phase purity of all samples were identified by an X-ray diffractometer (Beijing PGENERAL), which worked with Cu K $\alpha$  radiation ( $\lambda = 0.15406$  nm) and operated at 36 kV tube voltage and 20 mA tube current, respectively. Static and dynamic PL spectra at the temperature range of 25-300 °C were recorded on an Edinburgh PLS 920 fluorescence spectrometer. A 450 W Xenon lamp was used as the excitation source. The excitation photons for the decay curves were provided by a 60 W F900 flash lamp. The Xe lamp power, working voltage, scanning step, excitation and emission slits were set up to 150 W, 400 V, 1 nm, and 1.5 nm, respectively. All PL curves were corrected

over the lamp intensity with a silicon photodiode and further normalized by the PMT spectral response. The TL glow curves were recorded by a FJ427A1 TL dosimeter (CNNC Beijing Nuclear Instrument Factory), with a  $50\text{ }^{\circ}\text{C}\cdot\text{min}^{-1}$  heating rate. Prior to the TL measurement, the as-selected sample was irradiated by a 365 nm UV mercury vapor lamp for 1 min.

### 2.3 Theoretical Details

We used the CASTEP code to perform our DFT +  $U$  calculations with PBE functional [44-45]. The geometry optimization used the Broyden-Fletcher-Goldfarb-Shannon (BFGS) algorithm throughout all calculations. The unit cell for the  $\text{Sr}_3\text{Al}_2\text{O}_5\text{Cl}_2$  compound was built with 48 atoms inside. The kinetic cutoff energy was set to 750 eV with the valence electron states expressed in a plane-wave basis set. The ensemble DFT (EDFT) method of Marzari *et al* [46] was used for convergence. The supercell of the model was chosen to  $2 \times 2 \times 2$ . The reciprocal space integration was performed using the Gamma special  $k$ -point with Balderischi offset [47]. With these special  $k$ -points, the total energy was converged to less  $5.0 \times 10^{-7}$  eV per atom. The Hellmann-Feynman forces on the atom were converged to less than 0.001 eV/Å.

As for the pseudopotentials, the non-linear core corrected norm-conserving pseudopotential could provide a better response in the DFT +  $U$  calculations, especially for the calculations of RE doping [48]. This could help us to reflect all-electron behavior of the valence electrons, especially for the subtle effect of the  $4f/5d$  electrons and outer  $6s$  electrons of RE dopants (Tb, Eu). The Tb and Eu norm-conserving pseudopotentials were generated by using the OPIUM code in the Kleinman-Bylander projector form [49]. The non-linear partial core correction [50] and a scalar relativistic averaging scheme [51] were used to treat the spin-orbital coupling effect. For this treatment, the non-linear core correction technique was chosen for correcting the valence-core charge density overlapping in such heavy fermions elements. In particular, the ( $5s$ ,  $5p$ ,  $5d$ ,  $4f$ ,  $6s$ ,  $6p$ ) states were treated as the valence states of both Tb and Eu atoms. The RRKJ method was chosen for the optimization of the pseudopotentials [48, 52-53].

## 3. RESULTS AND DISCUSSION

### 3.1 Analysis on phase-purity and elemental homogeneity of $\text{Tb}^{3+}$ and $\text{Eu}^{3+}$ doped samples

The X-ray powder diffraction (XRD) profiles of four as-prepared samples, *i.e.*, bulk  $\text{Sr}_3\text{Al}_2\text{O}_5\text{Cl}_2$ ,  $\text{Sr}_{2.97}\text{Al}_2\text{O}_5\text{Cl}_2:3.0\%\text{Tb}^{3+}$ ,  $\text{Sr}_{2.97}\text{Al}_2\text{O}_5\text{Cl}_2:3.0\%\text{Eu}^{3+}$ , and  $\text{Sr}_{2.965}\text{Al}_2\text{O}_5\text{Cl}_2:1.5\%\text{Tb}^{3+},2.0\%\text{Eu}^{3+}$ , have been depicted in **Figure 1(c)**. Obviously, the  $\text{Eu}^{3+}$  and  $\text{Tb}^{3+}$  contents are the maximum nominal

content we experimentally designed in the  $\text{Sr}_3\text{Al}_2\text{O}_5\text{Cl}_2$  crystal host. After comparing the XRD peaks of these samples to those derived from the ICSD file No. 68365, we can easily conclude the as-prepared samples belong to an orthorhombic structure with the space group  $P2_12_12_1$ .

When compared to the nanoparticle achieved by the synthetic routines such as hydrothermal (*e.g.*,  $\text{KZnF}_3:\text{Mn}^{2+}$  [54]) and solvent-thermal method (*e.g.*,  $\text{NaYF}_4$ -based [55-56], and  $\text{NaGdF}_4$ -based core-shell nanocrystals [57]), the solid-state reaction method easily leads to the irregularly-shaped particles at the micrometer size level (*e.g.*,  $\text{K}_{1-x}\text{Na}_x\text{Sr}_{0.995}\text{PO}_4:0.005\text{Eu}^{2+}$  ( $0 \leq x \leq 0.6$ ) [14], and  $\text{Y}_3\text{Al}_5\text{O}_{12}:\text{Re}^{3+}$  ( $\text{Re}=\text{Ce}, \text{Sm}, \text{Tb}$ ) [58]). As a result, the inhomogeneity induced by the elemental aggregation may appear and influence the luminescent properties of phosphors accordingly. In this case, we have randomly selected one particle of  $\text{Sr}_{2.965}\text{Al}_2\text{O}_5\text{Cl}_2:1.5\%\text{Tb}^{3+}, 2.0\%\text{Eu}^{3+}$  to record the elemental mapping pattern (**Figure 1(d)**). Clearly, the particle consists of six elements (*i.e.*, Sr, Al, O, Cl, Tb and Eu), and all of them are homogeneously distributed, without any detectable element aggregation and phase separation. Hence, although multi sites are available for the  $\text{Tb}^{3+}$  and  $\text{Eu}^{3+}$  substitution, they do not induce the elemental aggregation.

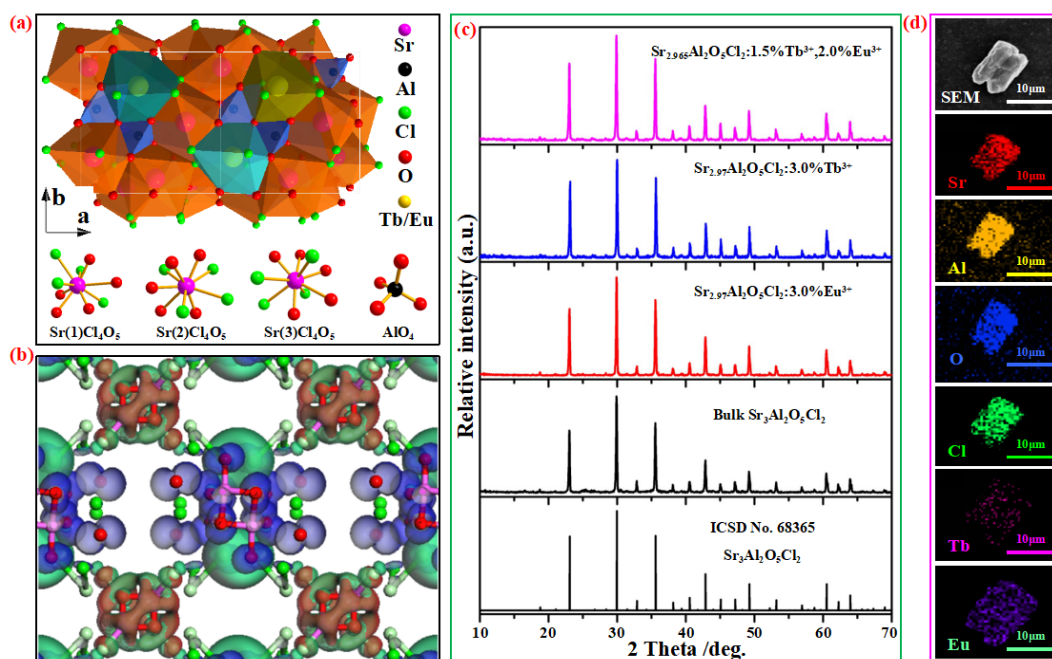


**Figure 1** (a) Double lattice cell of  $\text{Sr}_3\text{Al}_2\text{O}_5\text{Cl}_2$  and the Sr and Al coordination environments, which are drawn on the basis of ICSD card file No. 68365; (b) Orbital contour plots of VBM and CBM states, as well as gap states (Sr: green, Al: pink, Cl: light green, O: red, VBM: transparent blue, CBM: transparent green, and the intrinsic lattice induced gap states: transparent brown); (c) XRD patterns of bulk  $\text{Sr}_3\text{Al}_2\text{O}_5\text{Cl}_2$ ,  $\text{Sr}_{2.965}\text{Al}_2\text{O}_5\text{Cl}_2:1.5\%\text{Tb}^{3+}, 2.0\%\text{Eu}^{3+}$ ,  $\text{Sr}_{2.97}\text{Al}_2\text{O}_5\text{Cl}_2:3.0\%\text{Tb}^{3+}$ , and  $\text{Sr}_{2.97}\text{Al}_2\text{O}_5\text{Cl}_2:3.0\%\text{Eu}^{3+}$  samples; (d) Elemental mapping distribution of one representative particle randomly selected from the sample of  $\text{Sr}_{1.965}\text{Al}_2\text{O}_5\text{Cl}_2:1.5\%\text{Tb}^{3+}, 2.0\%\text{Eu}^{3+}$ .

### 3.2 Static and dynamic PL analysis

Since bulk  $\text{Sr}_3\text{Al}_2\text{O}_5\text{Cl}_2$  sample cannot emit the light upon excitation at any wavelengths, we had only measured the PL spectra of  $\text{Sr}_3\text{Al}_2\text{O}_5\text{Cl}_2:\text{Tb}^{3+}$ ,  $\text{Sr}_3\text{Al}_2\text{O}_5\text{Cl}_2:\text{Eu}^{3+}$  and  $\text{Sr}_3\text{Al}_2\text{O}_5\text{Cl}_2:\text{Tb}^{3+},\text{Eu}^{3+}$  phosphors. **Figure 2** shows the emission and excitation spectra of three typical samples, namely,  $\text{Sr}_{2.985}\text{Al}_2\text{O}_5\text{Cl}_2:1.5\%\text{Tb}^{3+}$ ,  $\text{Sr}_{2.99}\text{Al}_2\text{O}_5\text{Cl}_2:1.0\%\text{Eu}^{3+}$  and  $\text{Sr}_{2.725}\text{Al}_2\text{O}_5\text{Cl}_2:1.5\%\text{Tb}^{3+},1.25\%\text{Eu}^{3+}$ . It is obvious that the emission lines of the  $\text{Sr}_{2.985}\text{Al}_2\text{O}_5\text{Cl}_2:1.5\%\text{Tb}^{3+}$  sample upon excitation at 376 nm locate at 414 nm, 437 nm, 489 nm, 544 nm, 584 nm, and 623 nm (**Figure 2(a)**), corresponding to the  $^5\text{D}_3 \rightarrow ^7\text{F}_5$ ,  $^5\text{D}_3 \rightarrow ^7\text{F}_4$ ,  $^5\text{D}_4 \rightarrow ^7\text{F}_6$ ,  $^5\text{D}_4 \rightarrow ^7\text{F}_5$ ,  $^5\text{D}_4 \rightarrow ^7\text{F}_4$  and  $^5\text{D}_4 \rightarrow ^7\text{F}_3$  transitions of  $\text{Tb}^{3+}$  ions, respectively. The dominated  $\text{Tb}^{3+}$  emission lines at 489 nm and 544 nm can allow the  $\text{Tb}^{3+}$  doped  $\text{Sr}_3\text{Al}_2\text{O}_5\text{Cl}_2$  samples to exhibit the green color. Upon monitoring at 544 nm, the  $\text{Tb}^{3+}$  emission intensity as the  $\text{Tb}^{3+}$  doping content increases experiences an initial increase and a subsequent decrease, showing the optimal  $\text{Tb}^{3+}$  content that corresponds to the maximum emission intensity is 1.5% (the inset of **Figure 2(a)**). Similar to the  $\text{Sr}_3\text{Al}_2\text{O}_5\text{Cl}_2:\text{Tb}^{3+}$  samples,  $\text{Eu}^{3+}$  doped  $\text{Sr}_3\text{Al}_2\text{O}_5\text{Cl}_2$  sample also features several sharp emission lines (**Figure 2(b)**). Exciting at 393 nm enables two dominated  $\text{Eu}^{3+}$  lines at 616 and 592 nm, which corresponds to the electric dipole  $^5\text{D}_0 \rightarrow ^7\text{F}_2$  and magnetic dipole  $^5\text{D}_0 \rightarrow ^7\text{F}_1$  transitions of  $\text{Eu}^{3+}$ , respectively. This indicates the  $\text{Sr}_3\text{Al}_2\text{O}_5\text{Cl}_2:\text{Eu}^{3+}$  phosphors can serve as the red-emitting component. Upon monitoring at the emission intensity at 616 nm (inset of **Figure 2(b)**), the optimal  $\text{Eu}^{3+}$  content can be determined to be 1.0%.

The excitation spectra of  $\text{Sr}_{2.985}\text{Al}_2\text{O}_5\text{Cl}_2:1.5\%\text{Tb}^{3+}$  and  $\text{Sr}_{2.99}\text{Al}_2\text{O}_5\text{Cl}_2:1.0\%\text{Eu}^{3+}$  samples, which are monitored respectively at the wavelengths of 544 nm and 616 nm, are depicted in **Figure 2(c)**. The  $\text{Sr}_{2.985}\text{Al}_2\text{O}_5\text{Cl}_2:1.5\%\text{Tb}^{3+}$  sample exhibits a series of excitation lines within the spectral range of 250-500 nm, *i.e.*, 286 nm ( $^7\text{F}_6 \rightarrow ^5\text{H}_6$ ), 317 nm ( $^7\text{F}_6 \rightarrow ^5\text{H}_7$ ), 340 nm ( $^7\text{F}_6 \rightarrow ^5\text{G}_2$ ), 352 nm ( $^7\text{F}_6 \rightarrow ^5\text{D}_2$ ), 359 nm ( $^7\text{F}_6 \rightarrow ^5\text{G}_5$ ), 368 nm ( $^7\text{F}_6 \rightarrow ^5\text{G}_6$ ), 376 nm ( $^7\text{F}_6 \rightarrow ^5\text{D}_3$ ), and 486 nm ( $^7\text{F}_6 \rightarrow ^5\text{D}_4$ ). The  $\text{Sr}_{2.99}\text{Al}_2\text{O}_5\text{Cl}_2:1.0\%\text{Eu}^{3+}$  sample also shows several sharp excitation lines, *i.e.*, 322 nm ( $^7\text{F}_0 \rightarrow ^5\text{H}_6$ ), 362 nm ( $^7\text{F}_0 \rightarrow ^5\text{D}_4$ ), 381 nm ( $^7\text{F}_0 \rightarrow ^5\text{G}_4$ ), 393 nm ( $^7\text{F}_0 \rightarrow ^5\text{L}_6$ ), 415 nm ( $^7\text{F}_0 \rightarrow ^5\text{D}_3$ ), 464 nm ( $^7\text{F}_0 \rightarrow ^5\text{D}_2$ ), and 534 nm ( $^7\text{F}_0 \rightarrow ^5\text{D}_1$ ). On basis of the  $\text{Tb}^{3+}$  emission spectra (**Figure 2(a)**) and the  $\text{Eu}^{3+}$  excitation spectra (**Figure 2(c)(curve 2)**), we can observe a significant spectral overlapping between the  $\text{Eu}^{3+}$ -related excitation line (*i.e.*, 534 nm) and  $\text{Tb}^{3+}$ -related emission lines (*e.g.*, 544 nm), which, together with the excitation spectral overlapping between the  $\text{Eu}^{3+}$  and  $\text{Tb}^{3+}$  ions within the of 370-390 nm (**Figure 2(c)**), indicates the existence of the energy transfer from  $\text{Tb}^{3+}$  to

Eu<sup>3+</sup> ions. To verify it, we measured the emission spectra of Sr<sub>2.985-z</sub>Al<sub>2</sub>O<sub>5</sub>Cl<sub>2</sub>:1.5%Tb<sup>3+</sup>,zEu<sup>3+</sup> (z = 0.25%, 0.5%, 0.75%, 1.0%, 1.25%, 1.5%, 1.75%, 2.0%) samples. As expected, upon excitation at 376 nm results in simultaneous emissions of Tb<sup>3+</sup> and Eu<sup>3+</sup> ions (**Figure 2(d)**). The Eu<sup>3+</sup> emission intensity as the Eu<sup>3+</sup> content increases shows an initial increase and a subsequent decrease, which indicates the Eu<sup>3+</sup> content corresponding to the maximum emission intensity is 1.25% (the inset of **Figure 2(d)**). Unlike Eu<sup>3+</sup>, the Tb<sup>3+</sup> as the Eu<sup>3+</sup> content increases shows a continuous decrease in its emission intensity. Such emission intensity change upon excitation at 376 nm is a vivid spectral proof for the energy transfer from Tb<sup>3+</sup> to Eu<sup>3+</sup>. More importantly, due to the intrinsic behavior of the well-shielded 4f electrons configuration, both Tb<sup>3+</sup> and Eu<sup>3+</sup> emissions can keep the same PL position and sharp, without being affected by the Tb<sup>3+</sup> and Eu<sup>3+</sup> doping content, allowing the Tb<sup>3+</sup> and Eu<sup>3+</sup> ions to remain their respective green and red color purity.

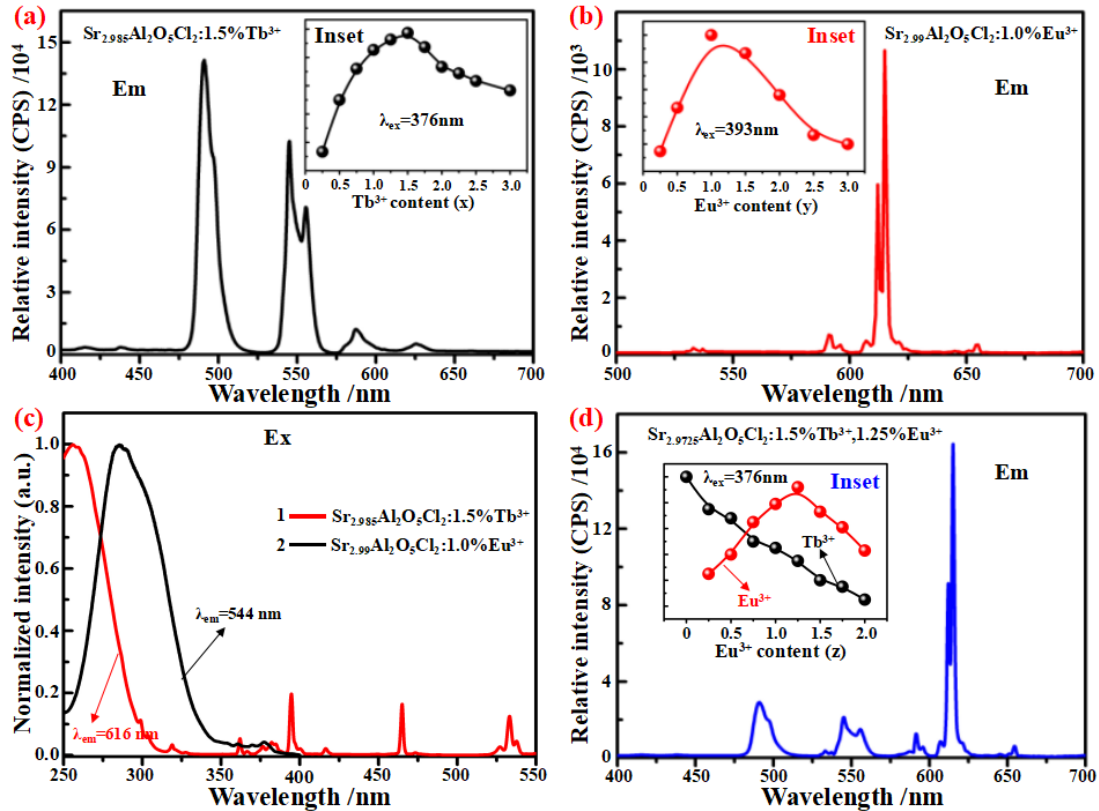


**Figure 2** Emission spectra of Sr<sub>2.985</sub>Al<sub>2</sub>O<sub>5</sub>Cl<sub>2</sub>:1.5%Tb<sup>3+</sup> and Sr<sub>2.99</sub>Al<sub>2</sub>O<sub>5</sub>Cl<sub>2</sub>:1.0%Eu<sup>3+</sup> samples upon excitation at 376 nm (a) and 393 nm (b), the doping content dependent emission intensity (**Inset**); (c) Excitation spectra of Sr<sub>2.985</sub>Al<sub>2</sub>O<sub>5</sub>Cl<sub>2</sub>:1.5%Tb<sup>3+</sup> and Sr<sub>2.99</sub>Al<sub>2</sub>O<sub>5</sub>Cl<sub>2</sub>:1.0%Eu<sup>3+</sup> samples upon monitoring at the wavelengths of 544 nm and 616 nm; (d) Emission spectra of the typical Sr<sub>2.9725</sub>Al<sub>2</sub>O<sub>5</sub>Cl<sub>2</sub>:1.5%Tb<sup>3+</sup>,1.25%Eu<sup>3+</sup> sample upon excitation at 376 nm, and the Eu<sup>3+</sup> content dependent Tb<sup>3+</sup> and Eu<sup>3+</sup> emission intensity (**Inset**).

To further reveal the underlying energy transfer mechanism, we have measured the decay curves of  $\text{Sr}_{2.985-z}\text{Al}_2\text{O}_5\text{Cl}_2:1.5\%\text{Tb}^{3+},z\text{Eu}^{3+}$  ( $z = 0.25\%, 0.5\%, 0.75\%, 1.0\%, 1.25\%, 1.5\%, 1.75\%, 2.0\%$ ) samples by using respectively 376 nm and 544 nm as the excitation and monitoring wavelengths (**Figure 3(a)**). All the decay curves can be fitted well by a double-exponential decay equation described as  $I(t) = A_1\exp(-t/\tau_1) + A_2\exp(-t/\tau_2)$  ( $\tau_1$  and  $\tau_2$  are short- and long-decay components, respectively, parameters  $A_1$  and  $A_2$  are the fitting constants) [14, 19, 41]. With the equation, *i.e.*,  $\tau = (A_1\tau_1^2 + A_2\tau_2^2)/(A_1\tau_1 + A_2\tau_2)$ , the average  $\text{Tb}^{3+}$ -related lifetimes, which correspond to the  $\text{Eu}^{3+}$  content of  $z = 0, 0.25\%, 0.5\%, 0.75\%, 1.0\%, 1.25\%, 1.5\%, 1.75\%$  and  $2.0\%$ , respectively, can be determined to be 3.195 ms, 2.603 ms, 1.968 ms, 1.425 ms, 1.221 ms, 0.951 ms, 0.673 ms, 0.633 ms, and 0.598 ms. Obviously, the rapid decrease of  $\text{Tb}^{3+}$  lifetimes with increasing the  $\text{Eu}^{3+}$  content reveals the existence of the energy transfer from  $\text{Tb}^{3+}$  to  $\text{Eu}^{3+}$  ions (**Figure 3(b)(curve 1)**).

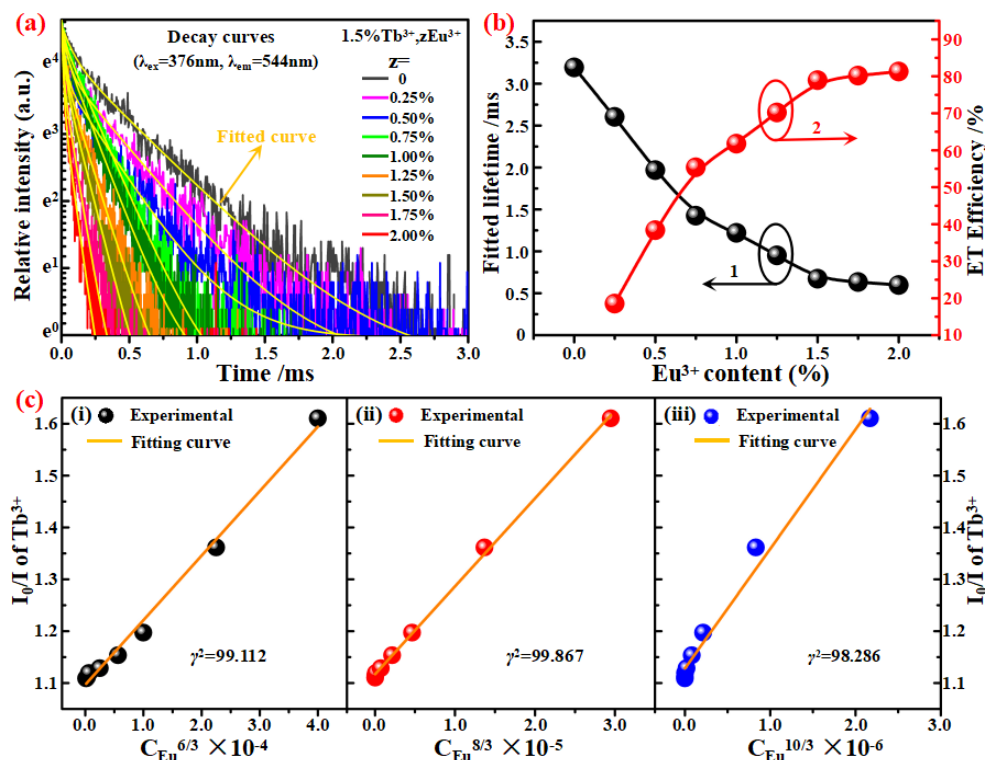


**Figure 3** (a) Decay curves ( $\lambda_{\text{ex}} = 376$  nm,  $\lambda_{\text{em}} = 544$  nm) of  $\text{Sr}_{2.985-z}\text{Al}_2\text{O}_5\text{Cl}_2:1.5\%\text{Tb}^{3+},z\text{Eu}^{3+}$  ( $z = 0, 0.25\%, 0.5\%, 0.75\%, 1.0\%, 1.25\%, 1.5\%, 1.75\%, 2.0\%$ ); (b) Dependence of  $\text{Tb}^{3+}$  lifetimes (**curve 1**) and energy transfer efficiencies ( $\eta_T$ ) (**curve 2**) on the  $\text{Eu}^{3+}$  content; (c) Dependence of  $I_0/I - C^n$  in the  $\text{Sr}_{2.985-z}\text{Al}_2\text{O}_5\text{Cl}_2:1.5\%\text{Tb}^{3+},z\text{Eu}^{3+}$  samples,  $n = 6$  (i), 8 (ii), and 10 (iii), respectively.

According to the as-obtained  $\text{Tb}^{3+}$  lifetimes, we can further calculate the energy transfer efficiency ( $\eta_T$ ) by using the expression [30, 38, 58-59]:  $\eta_T = 1 - \tau/\tau_0$  ( $\eta_T$  is the calculated energy transfer

efficiency, parameters  $\tau_0$  and  $\tau$  are the lifetimes of  $\text{Tb}^{3+}$  in the absence and presence of  $\text{Eu}^{3+}$ , respectively). As a result, a series of  $\eta_T$  values, *i.e.*, 18.53%, 38.40%, 55.40%, 61.78%, 70.23%, 78.94%, 80.19%, and 81.28%, which correspond to  $z = 0.25\%$ , 0.5%, 0.75%, 1.0%, 1.25%, 1.5%, 1.75% and 2.0%, respectively, can be achieved. Clearly, increasing the  $\text{Eu}^{3+}$  content leads to the increase of the energy transfer efficiency (**Figure 3(b)(curve 2)**), but such efficiency, typically at a low  $\text{Eu}^{3+}$  doping content, is not very efficiency. For example, the  $\eta_T$  values at the  $\text{Eu}^{3+}$  contents of 0.25% and 0.5% are only 18.53% and 38.40%, respectively, indicating not all the energy absorbed by  $\text{Tb}^{3+}$  can be re-absorbed by  $\text{Eu}^{3+}$  ions. The  $\eta_T$  value even at the  $\text{Eu}^{3+}$  doping content of 2.0% still cannot reach 100% (it is about only 81.28%). It would not be desirable if one wants to enhance the  $\text{Eu}^{3+}$  emission intensity by co-doping  $\text{Tb}^{3+}$  ions, but the inefficiency energy transfer is important for simultaneous achievement of  $\text{Tb}^{3+}$  and  $\text{Eu}^{3+}$  emissions.

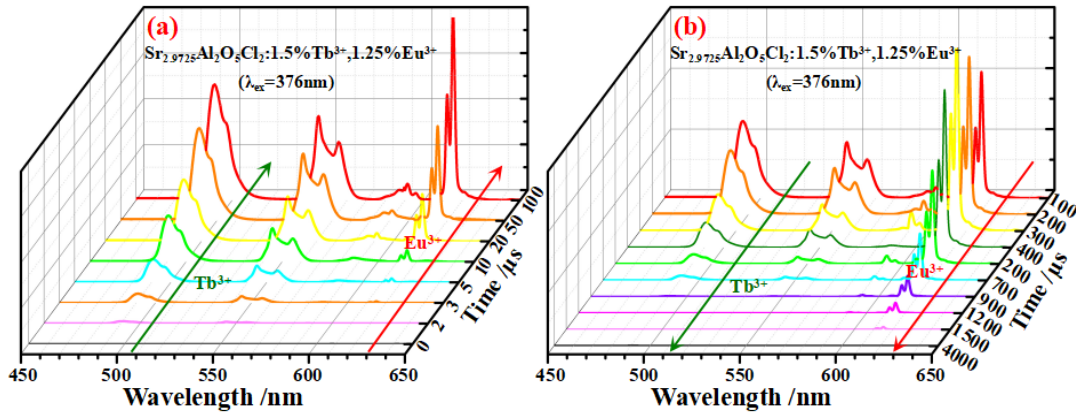


**Figure 4** Time-resolved PL spectra of  $\text{Sr}_{2.9725}\text{Al}_2\text{O}_5\text{Cl}_2:1.5\%\text{Tb}^{3+},1.25\%\text{Eu}^{3+}$  sample upon excitation at 376 nm. The decay time is collected spanning from 0 to 4 ms.

According to the *Dexter's* energy transfer expression of multi-polar interaction and *Reisfeld's* approximation, the below equation can be used to evaluate the energy transfer mechanism [60-61]:

$$\frac{\eta_0}{\eta} \propto C^{n/3} \quad (1)$$

where parameters  $\eta_0$  and  $\eta$  denote the luminescence quantum efficiencies of  $\text{Tb}^{3+}$  in the absence and presence of  $\text{Eu}^{3+}$ , respectively;  $C$  is the  $\text{Eu}^{3+}$  doping content;  $n = 6, 8,$  and  $10$  correspond to the dipole-dipole ( $d-d$ ), dipole-quadrupole ( $d-q$ ), and quadrupole-quadrupole ( $q-q$ ) interactions, respectively. Normally, the  $\eta_0/\eta$  ratio can be approximately estimated by their luminescence intensity ( $I_0/I$ ). Hence, a relationship between  $I_0/I$  and  $C^{n/3}$  can be draw (**Figure 3(c)**) and, on the

basis of the correlation coefficients, allows us to know that the energy transfer from  $\text{Tb}^{3+}$  to  $\text{Eu}^{3+}$  ions is happened via the  $d-q$  interaction rather than the  $d-d$  and  $q-q$  interactions.

### 3.3 Time-resolved PL analysis

For the  $\text{Sr}_{2.9875}\text{Al}_2\text{O}_5\text{Cl}_2:1.25\%\text{Eu}^{3+}$  and  $\text{Sr}_{2.985}\text{Al}_2\text{O}_5\text{Cl}_2:1.5\%\text{Tb}^{3+}$  samples, upon excitation at the wavelength of 376 nm can only allow them to exhibit the  $\text{Eu}^{3+}$  and  $\text{Eu}^{3+}$  emissions. With the above-proved energy transfer, we selected the  $\text{Sr}_{2.9725}\text{Al}_2\text{O}_5\text{Cl}_2:1.5\%\text{Tb}^{3+},1.25\%\text{Eu}^{3+}$  as the typical sample to measure the dynamic time-resolved PL spectra (**Figure 4**) and study the energy transfer from  $\text{Tb}^{3+}$  to  $\text{Eu}^{3+}$  ions. The reason why we selected the  $\text{Sr}_{2.9725}\text{Al}_2\text{O}_5\text{Cl}_2:1.5\%\text{Tb}^{3+},1.25\%\text{Eu}^{3+}$  is because the maximum  $\text{Eu}^{3+}$  emission intensity is at doping content of 1.25%, but the energy transfer efficiency (*i.e.*, 70.23%) is not neither the maximum nor the lowest value, which covers all PL possibilities we want to discuss. Considering the excitation wavelength and the  $\text{Eu}^{3+}$  and  $\text{Tb}^{3+}$  lifetimes (the  $\text{Eu}^{3+}$  lifetime in the  $\text{Sr}_3\text{Al}_2\text{O}_5\text{Cl}_2$  crystal lattice is about 756.12  $\mu\text{s}$  but not shown here), the 376 nm and 0 - 4 ms are selected as the excitation wavelength and the collected delay time range, respectively. In **Figure 4**, with increasing the delay time ( $t$ ) from 0 to 4 ms, the  $\text{Tb}^{3+}$  exhibits an initial increase and a subsequent decrease in its emission intensity. The delay time that corresponds to the maximum  $\text{Tb}^{3+}$  emission intensity is 100  $\mu\text{s}$ . As for  $\text{Eu}^{3+}$ , we can only detect its emission until the delay time ( $t$ ) is greater than 5  $\mu\text{s}$ . After that, the  $\text{Eu}^{3+}$  emission intensity as the delay time ( $t$ ) increases will increase continuously and then decrease, the tendency of which is very similar to that of  $\text{Tb}^{3+}$ . When the delay time ( $t$ ) is 300  $\mu\text{s}$ , the  $\text{Eu}^{3+}$  emission reaches the maximum intensity. Both  $\text{Tb}^{3+}$  and  $\text{Eu}^{3+}$  emissions after exceeding their respective maximum intensity will decrease continuously until their intensity disappear.

After comparing the lifetime of 756.12  $\mu\text{s}$  (for  $\text{Sr}_{2.9875}\text{Al}_2\text{O}_5\text{Cl}_2:1.25\%\text{Eu}^{3+}$ ) with that of 3.85 ms (for  $\text{Sr}_{2.985}\text{Al}_2\text{O}_5\text{Cl}_2:1.5\%\text{Tb}^{3+}$ ), we can easily notice that the  $\text{Eu}^{3+}$  lifetime is much greater than the  $\text{Tb}^{3+}$  lifetime. In this case, the time-resolved PL results can be used to discuss the dynamic energy transfer interaction between  $\text{Tb}^{3+}$  and  $\text{Eu}^{3+}$  ions. Although both  $\text{Tb}^{3+}$  and  $\text{Eu}^{3+}$  ions exist in the  $\text{Sr}_3\text{Al}_2\text{O}_5\text{Cl}_2$ , exciting at the wavelength of  $\text{Tb}^{3+}$  (*i.e.*, 376 nm) can only pump the  $\text{Tb}^{3+}$  emission. Prior to release of the absorbed energy,  $\text{Tb}^{3+}$  ions need some time to absorb the energy. And thus, it is reasonable that we cannot detect the  $\text{Tb}^{3+}$  emission when the delay time ( $t$ ) is less than 2  $\mu\text{s}$  (**Figure 4(a)**). As the delay time ( $t$ ) proceeds, however, the energy absorbed by  $\text{Tb}^{3+}$  ions enables transferring to the adjacent  $\text{Eu}^{3+}$  ions and then pumping the  $\text{Eu}^{3+}$  emission. Of course, because the

energy absorbed by the  $\text{Tb}^{3+}$  ions cannot immediately transfer to the  $\text{Eu}^{3+}$  ions, it also needs time to irradiate this process. As a result, the  $\text{Eu}^{3+}$  emission cannot be detectable until the delay time ( $t$ ) is greater than or equal to 5  $\mu\text{s}$ . Since the lifetime of  $\text{Tb}^{3+}$  in the  $\text{Sr}_3\text{Al}_2\text{O}_5\text{Cl}_2$  host crystal is longer than that of  $\text{Eu}^{3+}$ , the  $\text{Tb}^{3+}$ -absorbed energy can continuously transfer to  $\text{Eu}^{3+}$  (even the delay time ( $t$ ) exceeds the  $\text{Eu}^{3+}$  lifetime). For example, at the 1500  $\mu\text{s}$  (which is greater than the  $\text{Eu}^{3+}$  lifetime of 756.12  $\mu\text{s}$ ), the time-resolved PL spectra still can exhibit the  $\text{Eu}^{3+}$  emission, thereby exhibiting the delay time of  $\text{Eu}^{3+}$  greater than the  $\text{Eu}^{3+}$  lifetime itself (**Figure 4(b)**). Since the energy transfer from  $\text{Eu}^{3+}$  to  $\text{Tb}^{3+}$  ions after proceeding a certain delay time ( $t$ ) is impossible to proceed infinitely, both  $\text{Eu}^{3+}$  and  $\text{Tb}^{3+}$  emissions will disappear eventually. Because the energy absorbed by the  $\text{Tb}^{3+}$  ions enables immediately transferring to the  $\text{Eu}^{3+}$  ions when the decay time ( $t$ ) exceeds 200  $\mu\text{s}$ , the decay times ( $t$ ) that correspond to the disappearance time of  $\text{Eu}^{3+}$  and  $\text{Tb}^{3+}$  emissions are 1200  $\mu\text{s}$  and 200  $\mu\text{s}$ , respectively. This disappearance of  $\text{Tb}^{3+}$  decay time ( $t$ ) shows much less than that of  $\text{Eu}^{3+}$ , exhibiting the disappearance of  $\text{Tb}^{3+}$  decay time ( $t$ ) is much less than itself lifetime. Hence, the time-resolved PL results indicate that the  $\text{Tb}^{3+}$  and  $\text{Eu}^{3+}$  present a completely different decay times ( $t$ ) as compared to their respective lifetimes.

Although some previously-reported works have involved the time-resolved PL spectra to study the energy transfer interactions, all of them are based on either the energy transfer from the host that features a shorter lifetime to a single dopant that features a longer lifetime (*e.g.*,  $\text{ScVO}_4:\text{Bi}^{3+}$  [41],  $\text{CaWO}_4:\text{Eu}^{3+}$  and  $\text{CaWO}_4:\text{Tb}^{3+}$  [42],  $\text{LuVO}_4:\text{Bi}^{3+}$  [43], and  $\text{ScVO}_4:\text{Eu}^{3+}$  [62]) or from one center to another luminescent center in a given crystal host (*e.g.*,  $\text{Sr}_2\text{P}_2\text{O}_7:\text{Bi}^{2+}$  [63]). In addition, the related works are still very limited after considering more than tens of thousands of rare earth (RE) and non-RE related photonic materials have been discovered in the past years. Unlike these works, we, for the first time, directly show the existence of the energy transfer from one dopant with a longer lifetime to another dopant with a shorter lifetime based on the time-resolved PL spectra. Since both  $\text{Eu}^{3+}$  and  $\text{Tb}^{3+}$  ions are featured with the well-shielded  $4f$  electrons configuration, our work enables providing some new directive ideas for researchers to use the time-resolved PL spectra to study the energy transfer interactions in other well-shielded  $4f$  electron RE (*e.g.*,  $\text{Eu}^{3+}$ ,  $\text{Er}^{3+}$  *etc*) and non-RE ions (*e.g.*,  $\text{Mn}^{4+}$ ,  $\text{Cr}^{3+}$  *etc*) doped systems that cover the visible and infrared region.

### **3.4 Temperature-dependent PL analysis**

In general, the PL properties of one phosphor at high temperature sometimes are different from

what we observe at room temperature, typically for those RE (*e.g.*,  $\text{Eu}^{2+}$ ,  $\text{Ce}^{3+}$ ) and non-RE (*e.g.*,  $\text{Bi}^{3+}$ ,  $\text{Mn}^{2+}$ ) phosphor materials with broad excitation and emission bands. For example, with the increase of temperature, the  $\text{BaAl}_2\text{Si}_2\text{O}_8:\text{Eu}^{2+}$  phosphor shows a blue-shift of  $\text{Eu}^{2+}$  position [64], the  $\text{Sr}_2\text{Si}_5\text{N}_8:\text{Eu}^{2+}$  exhibits simultaneous blue-shifting and red-shifting of  $\text{Eu}^{2+}$  emission [65], the  $\text{ScVO}_4:\text{Bi}^{3+}$  [25] and  $\text{KZnF}_3:\text{Mn}^{2+}$  [54] feature an initial enhancement of emission intensity.

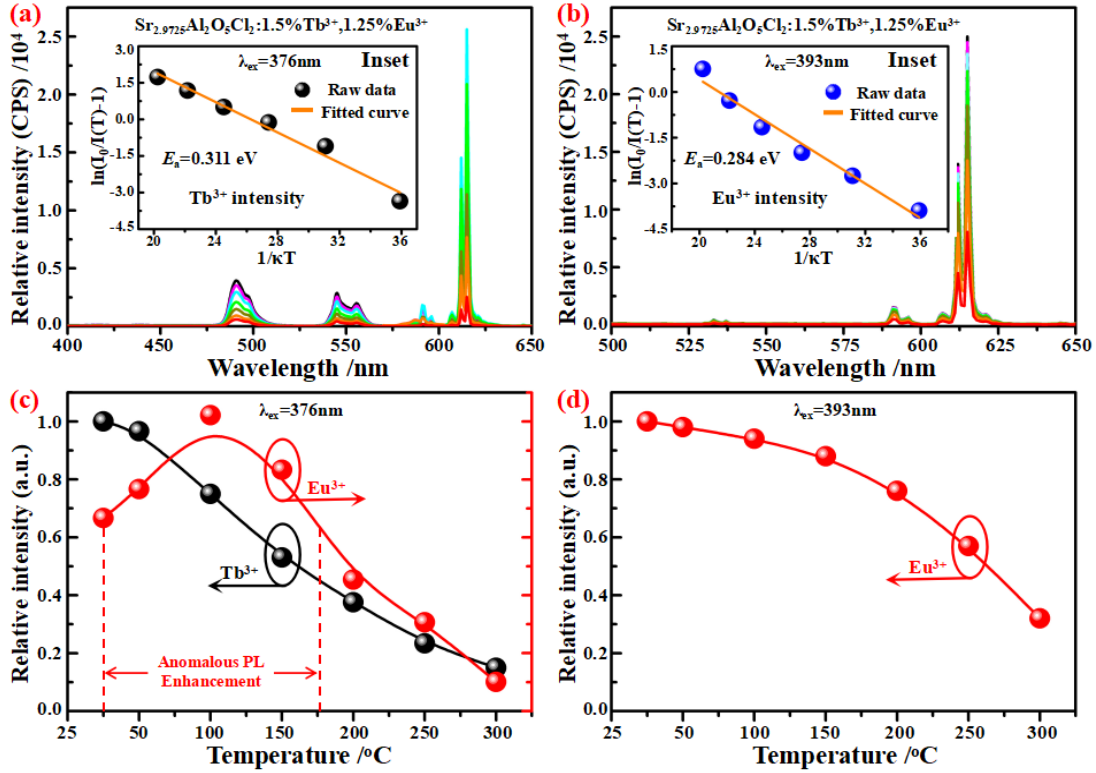


**Figure 5** Temperature-dependent emission spectra of the  $\text{Sr}_{2.9725}\text{Al}_2\text{O}_5\text{Cl}_2:1.5\%\text{Tb}^{3+},1.25\%\text{Eu}^{3+}$  sample upon excitation at 376 nm (a) and 393 nm (b), and the excitation wavelengths and the related linear fitting of the emission intensity at 544 nm and 616 nm have been also depicted in the inset; (c) and (d) are dependence of the emission intensity at 544 nm (*i.e.*, for  $\text{Tb}^{3+}$ ) and 616 nm (*i.e.*, for  $\text{Eu}^{3+}$ ) on the temperature upon excitation at 376 nm and 393 nm, respectively.

In order to check whether there are some hitherto unnoticed PL properties of the well-shielded 4f  $\text{Eu}^{3+}$  and  $\text{Tb}^{3+}$  ions in the  $\text{Sr}_3\text{Al}_2\text{O}_5\text{Cl}_2$  crystal host, here we have selected the typical sample of  $\text{Sr}_{2.9725}\text{Al}_2\text{O}_5\text{Cl}_2:1.5\%\text{Tb}^{3+},1.25\%\text{Eu}^{3+}$  to record the temperature-dependent emission spectra upon excitation at 376 nm (a) and 393 nm (b) (Figure 5). In the figure, increasing the temperature can simultaneously pump both  $\text{Tb}^{3+}$  and  $\text{Eu}^{3+}$  emissions, but their relative emission intensity upon the same heating process experiences a completely different process. The  $\text{Tb}^{3+}$ -related emission shows a continuous decrease in the intensity, while the  $\text{Eu}^{3+}$ -related emission intensity features an initial enhancement and a subsequent decrease (Figure 5(c)). Exciting at 393 nm, however, can only

pump the  $\text{Eu}^{3+}$  emission and its continuously-decreasing intensity (**Figure 5(b)** and **Figure 5(d)**). With these spectral information, we used the *Arrhenius* equation [43, 62], *i.e.*,  $I(T) = I_0/(1 + A\exp(-E_a/\kappa T))$  (where  $I_0$  is the initial emission intensity,  $I(T)$  is the intensity at a given temperature  $T$ ,  $A$  is a constant,  $E_a$  is the required activation energy for thermal quenching, and  $\kappa$  is the *Boltzmann's* constant ( $8.62 \times 10^{-5}$  eV)), to evaluate the activation energy ( $E_a$ ) for  $\text{Tb}^{3+}$  and  $\text{Eu}^{3+}$  emissions. To better acquire the  $E_a$  value, we need to transform this equation into the expression described as  $\ln[(I_0/I(T)) - 1] = \ln A - E_a/\kappa T$ . Based on the relationship between  $\ln[(I_0/I) - 1]$  and  $1/\kappa T$  (inset of **Figures 5(a-b)**), two  $E_a$  values, *i.e.*, 0.311 and 0.284 eV, which correspond respectively to the  $\text{Tb}^{3+}$  and  $\text{Eu}^{3+}$  emissions upon excitation at 376 nm and 393 nm, are achieved. Obviously, the two values are comparable to and/or less than some previous  $\text{Eu}^{3+}$  doped phosphors, such as 0.41 eV in  $\text{Sr}_4\text{Ge}_2\text{O}_7\text{F}_2:\text{Eu}^{3+}$  [66], 0.408 eV in  $\text{NaLa}_4[\text{MoO}_3\text{O}_{15}]\text{F}:\text{Eu}^{3+}$  [67], and 0.445 eV in  $\text{Y}_2\text{Ti}_2\text{O}_7:\text{Eu}^{3+}$  [68]. The thermal quenching temperatures,  $T_{50\%}$ , defining as the temperature at half of their initial emission intensity at room temperature, are determined to 150 °C and 190 °C, respectively. The  $\text{Eu}^{3+}$  emission intensity at 200 °C can remain ~76% of  $T_0 = 25$  °C, implying the as-obtained phosphors hold excellent PL resistance against the thermal quenching.

### 3.5 Analysis on the site occupancy preference by Rietveld refinement and DFT modeling

As for the temperature-induced anomalous  $\text{Eu}^{3+}$  PL properties in the  $\text{Tb}^{3+}$ ,  $\text{Eu}^{3+}$  doped  $\text{Sr}_3\text{Al}_2\text{O}_5\text{Cl}_2$  phosphor, the underlying reason we first felt may result from the site occupancy preference. This is because, on one hand, such PL phenomenon, typically upon excitation at the wavelength of other doping ions, is still seldom noticed by previous works, and on the other hand, it involves multi luminescent centers that feature the energy transfer process from one dopant with longer lifetime (*i.e.*,  $\text{Tb}^{3+}$ ) to another dopant with shorter lifetime (*i.e.*,  $\text{Tb}^{3+}$ ). To check the possibility, we have used the *FullProf* Suite Program to refine the raw XRD data of  $\text{Tb}^{3+}$ ,  $\text{Eu}^{3+}$  doped  $\text{Sr}_3\text{Al}_2\text{O}_5\text{Cl}_2$  samples. After considering the cationic radii of  $\text{Sr}^{2+}$  ( $R_{\text{CN}=9} = 1.31$  Å, CN denotes the coordination number),  $\text{Tb}^{3+}$  ( $R_{\text{CN}=9} = 1.095$  Å) and  $\text{Eu}^{3+}$  ( $R_{\text{CN}=9} = 1.12$  Å) ions, we first allowed  $\text{Tb}^{3+}$  and  $\text{Eu}^{3+}$  ions to substitute for  $\text{Sr}^{2+}$  sites. As a result, the final reliability factors, *i.e.*, profile factor  $R_p = 8.36\%$ , expected weighted profile factor  $R_{\text{exp}} = 5.79\%$ , crystallographic factor  $R_F = 2.71\%$ , Bragg factor  $R_{\text{Bragg}} = 3.65\%$ , indicator of goodness of fit  $\text{GOF} = 2.03$  and weighted profile factor  $R_{\text{wp}} = 7.03\%$ , are achieved. The Rietveld refinement profile and cell parameters are given in **Figure 6(a)** and **Table 2**. When compared to the cell parameters of  $a(b)(c)$  (*i.e.*, 9.4220 Å) and cell volume  $V$

(*i.e.*, 836.43 Å<sup>3</sup>) derived from the standard ICSD card file No. 68365, the refined parameters (*i.e.*,  $a(b)(c) = 9.3782 \text{ \AA}$ ,  $V = 824.819 \text{ \AA}^3$ ) show a slight shrinkage, indicating the possibility of the substitution of larger Sr with smaller Tb<sup>3+</sup> and Eu<sup>3+</sup>. However, what can make us surprising is the Tb<sup>3+</sup> doped Sr<sub>3</sub>Al<sub>2</sub>O<sub>5</sub>Cl<sub>2</sub> sample shows a completely different result as compared to that of Eu<sup>3+</sup> doped Sr<sub>3</sub>Al<sub>2</sub>O<sub>5</sub>Cl<sub>2</sub> sample. The refined parameters (*i.e.*,  $a(b)(c) = 9.5346 \text{ \AA}$ ,  $V = 899.778 \text{ \AA}^3$ ) of the former show a slight expansion, while the refined parameters (*i.e.*,  $a(b)(c) = 9.4017 \text{ \AA}$ ,  $V = 831.035 \text{ \AA}^3$ ) of the latter shows a slight shrinkage (**Table 2**). These indicate that Tb<sup>3+</sup> singly doped Sr<sub>3</sub>Al<sub>2</sub>O<sub>5</sub>Cl<sub>2</sub> sample obeys the general chemical point of view where the exotic doping ions should substitute the crystal ions that have the same or similar ionic radii as these exotic ions. However, considering the same valences (*i.e.*, +3) and the size differences (*i.e.*, CN = 9, 0.39 Å for Al<sup>3+</sup> ions, < 0.923 Å for Tb<sup>3+</sup> ions), significant expansion of cell lattice, inducing by substitution of Al<sup>3+</sup> with Tb<sup>3+</sup> ions, appears, as reflected by the refined results of Tb<sup>3+</sup> doped Sr<sub>3</sub>Al<sub>2</sub>O<sub>5</sub>Cl<sub>2</sub> sample (**Table 2**). To verify the possibility of substitution of smaller Al<sup>3+</sup> with larger Tb<sup>3+</sup> and larger Sr with smaller Eu<sup>3+</sup>, the DFT modeling is used here to further screen this type of substitution.

**Table 2** Rietveld refinement results for Sr<sub>2.965</sub>Al<sub>2</sub>O<sub>5</sub>Cl<sub>2</sub>:1.5%Tb<sup>3+</sup>,2.0%Eu<sup>3+</sup> (SACTE), Sr<sub>2.97</sub>Al<sub>2</sub>O<sub>5</sub>Cl<sub>2</sub>:3.0%Eu<sup>3+</sup> (SACE), and Sr<sub>2.97</sub>Al<sub>2</sub>O<sub>5</sub>Cl<sub>2</sub>:3.0%Tb<sup>3+</sup> (SACT) samples, reference data of Sr<sub>3</sub>Al<sub>2</sub>O<sub>5</sub>Cl<sub>2</sub> (SAC) are from ICSD standard card are also included for reference.

Items	SAC	SACTE	SACE	SACT
ICSD file no.	No. 68365	---	---	---
Crystal system		Orthorhombic		
Space group		<i>P2<sub>1</sub>2<sub>1</sub>2<sub>1</sub></i>		
Z		4		
Parameters ( <i>a,b,c</i> )/Å	9.4220	9.3782	9.4017	9.5346
Volume ( <i>V</i> )/Å <sup>3</sup>	836.43	824.819	831.035	899.778
Profile factor <i>R<sub>p</sub></i>	---	8.36%	11.28%	15.16%
Weighted profile factor <i>R<sub>wp</sub></i>	---	7.03%	9.39%	13.92%
Expected weighted profile factor <i>R<sub>exp</sub></i>	---	5.79%	8.31%	9.44%
Bragg factor <i>R<sub>Bragg</sub></i>	---	3.65%	5.67%	7.38%
Crystallographic factor <i>R<sub>F</sub></i>	---	2.71%	4.65%	6.51%
GOF	---	2.03	2.57	3.34

From the theoretical point, we performed the simple DFT calculations to consider the energetics of Eu and Tb substitution doping within the host lattice. We find the Eu prefers to substitute the Sr-site instead of occupying the Al site, and the formation energy has been given in the inset of

**Figure 6(b).** The contrast of the energy between the two sites is about 4 eV, and the host ion randomized distribution induced energetic error has been considered. Further on the Tb doping, it shows a different behavior when compared to the Eu doping. The Tb favors substituting the Al-site more than the Sr-site within the host. Overall, the  $Tb_{Sr}$  doping gives the highest energetic cost to form while the lowest energy of formation is the  $Tb_{Al}$ . Next, we move on to the thermodynamic transition energy level to compare the  $4f$ -charge transfer state with related to the  $E_F$  for the  $(0/3+)$  state (**Figure 6(b)**). We find both  $Eu_{Al}$  and  $Eu_{Sr}$  demonstrate a deep donor behavior closing to the valence band (VB) edge, where the 0 eV denotes the VB top. However, the  $Tb_{Al}$  is a relatively shallow donor since the transition energy level is close to the conduction band CB edge. Note that our estimated band gap is 3.0 eV, and may be underestimated without any orbital corrections. The  $Tb_{Sr}$  shows a similar deep donor behavior to the Eu doping cases.

We further perform on the energetic behaviors of different substitution doping in the host matrix. To illustrate the dependence of temperature on the free energy in the system, the thermodynamic principles are imported to discuss the stability. Firstly, we model that the as-discussed solid system can be seen as relatively ordered “solid-solution”. The related Gibbs free energy ( $G = H - TS$ ) can be provided, where the  $H$  is the standard formation enthalpy of the system at the temperature  $T$ , and the  $S$  is the system entropy. Under the constant pressure approximation, the change in free energy ( $\Delta G$ ) of the doped solid system with related to the ideal host matrix is given as following description:

$$\Delta G = \Delta E + \Delta ZPE - T\Delta S \quad (2)$$

where  $\Delta E$  is the total energy change for the defect formation, directly obtaining from our self-consistent DFT calculations,  $\Delta ZPE$  is the change in zero-point energies of the system compared to the ideal structure at the  $T = 0$ ,  $T$  is the “solid-solution” ambient temperature and  $\Delta S$  is the change in entropy for the whole system with consideration of extrinsic doping formation process. Introducing the important criterion, when the change in free energy of the system gets to:

$$\Delta G \leq 0 \quad (3)$$

This will have a spontaneous formation process for the specific defect, following the second thermodynamic law of physical chemistry. Herein, we have carried out the related calculations on the Tb and Eu doping respectively occur on the Al and Sr sites in the host system as shown in **Figure 6(c)**. The zero point energy of the Sr-Al-Cl-O solid solution system is found to be 2.24 eV.

When the extrinsic doping introduced, the local short-range disorder induced structural distortion further varies the zero-point energy (ZPE) of the solid-solution systems.

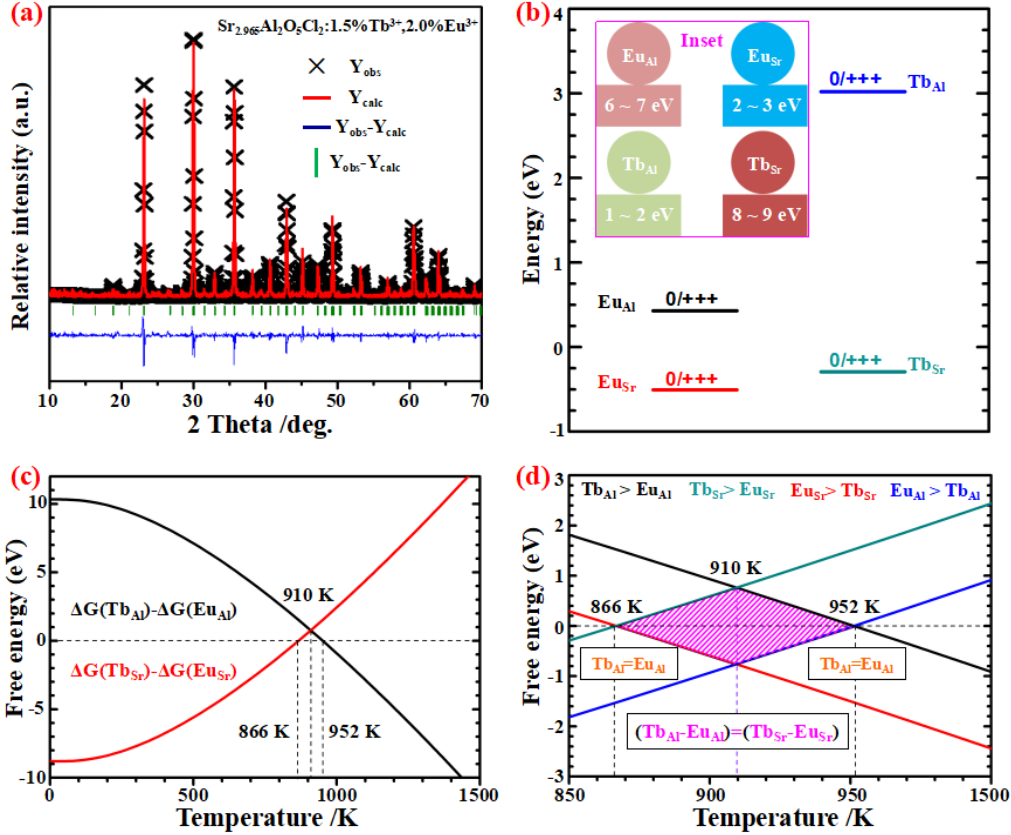


**Figure 6** (a) Refined XRD pattern (—) of  $\text{Sr}_{1.965}\text{Al}_2\text{O}_5\text{Cl}_2:1.5\%\text{Tb}^{3+}, 2.0\%\text{Eu}^{3+}$  sample, Rietveld refining results ( $\times$ ), Bragg reflections ( $\uparrow$ ) and the profile difference between observed and calculated values (—); (b) Thermodynamic transition energy for the transferring electrons from the neutral to tri-positively charged ionic state of Eu and Tb doping and Formation energy of neutral Eu and Tb substitution doping in the host matrix (inset); (c) Thermodynamic free energy changing trend for the Tb and Eu substitution doping in the host matrix; (d) The thermodynamic evolutions of the different energetic preferences by the Tb and Eu substitution doping

Considering the ground state formation enthalpies, the Tb and Eu substitution doping on the Sr and Al sites respectively can be updated with temperature dependence changing trends shown in **Figures 6(c-d)**. As we estimated based on this method, at the temperature lower than the 952 K, the  $\text{Eu}_{\text{Al}}$  doping shows more energetic favorable than the  $\text{Tb}_{\text{Al}}$  doping. This trend turns to be conversed when the temperature increases to the 952 K. For the Sr substituted doping, the  $\text{Tb}_{\text{Sr}}$  shows more stabilities than the  $\text{Eu}_{\text{Sr}}$  doping below the 866 K, and the reversed trend occurs when temperature is higher than 866 K. This indicates that, at the lower temperature in the synthesis, the  $\text{Tb}_{\text{Sr}}$  and  $\text{Eu}_{\text{Al}}$  doping can be easily formed and the formation energy at the 0 K of the  $\text{Tb}_{\text{Sr}}$  doping

shows even lower than  $\text{Eu}_{\text{Al}}$ . With using the  $E_q$  (2) as criterion, we noticed that the 910 K is the temperature critical turning point that gives the  $[\Delta G(\text{Tb}_{\text{Al}}) - \Delta G(\text{Eu}_{\text{Al}})] = [\Delta G(\text{Tb}_{\text{Sr}}) - \Delta G(\text{Eu}_{\text{Sr}})]$ . This implies the energetic contrast of Tb and Eu doping turns to be equivalent at that temperature point. With determination of the three temperature critical point, the pink shaded area (**Figure 6(d)**) represents the evolution of an energetic difference arise from the contrast of chemical potentials between Tb and Eu on different Sr and Al sites. Recalling the optimal synthesis temperature used in our work (1200 °C, *i.e.*, around 1500 K), both the  $\text{Tb}_{\text{Al}}$  and  $\text{Eu}_{\text{Sr}}$  doping show more dominant effects in the host matrix. It is obvious that our calculated temperatures are in a good agreement and consistency with the reported experimental data, indicating the current synthesis routes have already easily introduced the extrinsic co-doping behaviors of choosing different substitution sites (Sr or Al) by Eu and Tb and can be driven by the energetic preference in terms of change in free energy. We also illustrate the HOMO and LUMO charge densities contour plots on the host matrix system. As shown in **Figure 1(b)**, we find the Al-O local sub-lattice clearly bounds the electrons in order to form the valence band orbitals, while the Sr-Cl sub-lattice system contributes to the antibonding orbitals denotes the charge density arrangement by the conduction band.

### 3.6 Discussion on Tunable PL Observations

Re-inspection into the spectral results of **Figure 2** and **Figures 4-5**, increasing the  $\text{Eu}^{3+}$  content yet fixing the  $\text{Tb}^{3+}$  content enables controlling the energy transfer efficiency from  $\text{Tb}^{3+}$  to  $\text{Eu}^{3+}$ , and such energy transfer typically at low  $\text{Eu}^{3+}$  doping content is inefficient (**Figure 3(a-b)**), leading to simultaneous emissions of  $\text{Tb}^{3+}$  and  $\text{Eu}^{3+}$  and broad color tuning from green (0.3159, 0.5572) to red (0.6579, 0.3046) (**Figure 7(a-b)**). As for the temperature-dependent decay curves of typical  $\text{Sr}_{2.9725}\text{Al}_2\text{O}_5\text{Cl}_2:1.5\%\text{Tb}^{3+}, 1.25\%\text{Eu}^{3+}$  sample, they also can be fitted by the double-exponential decay equation of  $I(t) = A_1\exp(-t/\tau_1) + A_2\exp(-t/\tau_2)$ . A series of the average lifetimes of  $\text{Tb}^{3+}$  ions, as calculated from the equation of  $\tau = (A_1\tau_1^2 + A_2\tau_2^2)/(A_1\tau_1 + A_2\tau_2)$ , are determined to be 2.421 ms, 1.616 ms, 0.552 ms, 0.187 ms, 0.081 ms, and 0.036 ms, corresponding to 50 °C, 100 °C, 150 °C, 200 °C, 250 °C, and 300 °C, respectively (**Table 3**). It indicates a gradual decrease of  $\text{Tb}^{3+}$  lifetime with increasing the temperature. On the basis of the  $\eta_T = 1 - \tau/\tau_0$  equation, we can further evaluate the temperature-dependent  $\eta_T$  from  $\text{Tb}^{3+}$  to  $\text{Eu}^{3+}$ , and they are 24.23%, 49.42%, 82.72%, 94.15%, 97.46% and 98.87%, corresponding to 50 °C, 100 °C, 150 °C, 200 °C, 250 °C, and 300 °C, respectively. Within  $\leq 150$  °C, the  $\eta_T$  gap as the temperature increases becomes larger and larger,

such as, 24.23% between 25 °C and 50 °C, 25.19% between 50 °C and 100 °C, and 33.30% between 100 °C and 150 °C. It implies that the energy transfer from Tb<sup>3+</sup> to Eu<sup>3+</sup> ions has been accelerated with the help of the thermal stimulation. This accelerated energy transfer can be also reflected by the temperature-dependent PL intensity. The decreased gap of the Tb<sup>3+</sup> intensity at the earlier heating process (*i.e.*,  $\leq 150$  °C) also becomes larger and larger (**Figure 5(c)**).

**Table 3** Temperature-dependent lifetime of Sr<sub>3(0.985-z)Al<sub>2</sub>O<sub>5</sub>Cl<sub>2</sub>:1.5%Tb<sup>3+</sup>,1.25%Eu<sup>3+</sup> phosphors ( $\lambda_{\text{ex}} = 376$  nm,  $\lambda_{\text{em}} = 544$  nm)</sub>

Temperature /°C	50	100	150	200	250	300
$A_1$	282.83	341.85	437.37	418.36	792.45	863.44
$\tau_1$ /ms	0.461	0.412	0.231	0.055	0.041	0.021
$A_2$	679.44	612.01	542.29	575.88	227.85	140.91
$\tau_2$ /ms	2.567	1.772	0.645	0.212	0.126	0.065
$\tau_{\text{ave}}$ / ms	2.421	1.616	0.552	0.187	0.081	0.036

The Tb<sup>3+</sup> doped Sr<sub>3</sub>Al<sub>2</sub>O<sub>5</sub>Cl<sub>2</sub> phosphor upon excitation at the UV light can emit green afterglow luminescence [31-32], allowing us to record the thermoluminescence (TL) glow spectrum for the Sr<sub>2.9725</sub>Al<sub>2</sub>O<sub>5</sub>Cl<sub>2</sub>:1.5%Tb<sup>3+</sup>,1.25%Eu<sup>3+</sup> sample (**Figure 7(c)**). Three overlapping yet distinguishable TL bands, locating at 78 °C, 129 °C, and 256 °C, are observable. Except for the TL intensity, the three PL positions are basically inconsistent with those (*i.e.*, 62 °C, 142 °C, and 250 °C) reported by Chen *et al* in Tb<sup>3+</sup> doped Sr<sub>3</sub>Al<sub>2</sub>O<sub>5</sub>Cl<sub>2</sub> phosphor [32], which is due to the addition of Eu<sup>3+</sup> ions in Tb<sup>3+</sup> doped Sr<sub>3</sub>Al<sub>2</sub>O<sub>5</sub>Cl<sub>2</sub> phosphor. When taking into account the TL and temperature-induced Eu<sup>3+</sup>-related photoemission curve (**Figure 5(c)**), however, we can find that the two curves share with the same temperature range within 25-200 °C. As known, the TL properties usually are used to reflect the afterglow luminescence properties that relate to the carriers trapped and de-trapped by defects in the crystal lattices and thus, can reveal the traps status. Moreover, the defect-trapped electrons upon thermal stimuli can return to the energy levels of the excited state [69-70], which, as Kang *et al* and Meijerink *et al* show respectively in the LuVO<sub>4</sub>:Bi<sup>3+</sup> phosphor [43] and colloidal CdSe QDs [71-72], may contribute to enhancing the emission intensity during the heating process. In consequence, the temperature-triggered anti-quenching of luminescence appears. However, our current results after comparing to these reported works exhibit significant difference. The reported works involve either the QDs in the colloidal status or the energy transfer from the LuVO<sub>4</sub> host to

a single dopant (*i.e.*, Bi<sup>3+</sup>) (the LuVO<sub>4</sub> host itself can also show the luminescence). For this work, it involves two exotic dopants in the solid state powder, and the Sr<sub>3</sub>Al<sub>2</sub>O<sub>5</sub>Cl<sub>2</sub> host itself does not have the luminescence. In this case, a mechanistic profile, which bases on jointly taking into account the XRD Rietveld refinement, TL, PL and DFT, is proposed here to illustrate the color tuning and temperature-triggered Eu<sup>3+</sup>-related emission enhancement (**Figure 7(d)**). Specifically, with the aid of the <sup>7</sup>F<sub>6</sub> → <sup>5</sup>D<sub>3</sub> transition, the Tb<sup>3+</sup> ions first absorb the UV photons (*i.e.*, 376 nm) and then lift the photons from the ground state of <sup>7</sup>F<sub>6</sub> to a higher-energy excited state of <sup>5</sup>D<sub>3</sub>. Afterwards, some of the excited photons can directly transmit from the <sup>5</sup>D<sub>4</sub> level to the ground state of <sup>7</sup>F<sub>6</sub>, leading to the emissions dominated at 414 and 437 nm. Other excited Tb<sup>3+</sup> photons relax to the lower-energy excited state of <sup>5</sup>D<sub>4</sub> through non-radiative transition, leading to emissions at 489 nm (<sup>5</sup>D<sub>4</sub> → <sup>7</sup>F<sub>6</sub>), 544 nm (<sup>5</sup>D<sub>4</sub> → <sup>7</sup>F<sub>5</sub>), 584 nm (<sup>5</sup>D<sub>4</sub> → <sup>7</sup>F<sub>4</sub>), and 623 nm (<sup>5</sup>D<sub>4</sub> → <sup>7</sup>F<sub>3</sub>). When the Eu<sup>3+</sup> ions are co-doped into, the energy emitted from the Tb<sup>3+</sup> ions can be reabsorbed by Eu<sup>3+</sup> ions due to the spectral overlapping between the Tb<sup>3+</sup> 544 nm (<sup>5</sup>D<sub>4</sub> → <sup>7</sup>F<sub>5</sub>) emission and Eu<sup>3+</sup> 534 nm (<sup>7</sup>F<sub>0</sub> → <sup>5</sup>D<sub>1</sub>) excitation. As a result, upon excitation at the excitation wavelength of Tb<sup>3+</sup> (*i.e.*, 376 nm) enables pumping the Eu<sup>3+</sup> emissions. Due to the controllable energy transfer efficiency, the Sr<sub>3</sub>Al<sub>2</sub>O<sub>5</sub>Cl<sub>2</sub>:Tb<sup>3+</sup>,Eu<sup>3+</sup> samples upon excitation at 376 nm can simultaneously exhibit the Tb<sup>3+</sup> and Eu<sup>3+</sup> emissions with different intensity. As a result, the tunable emission colors, resulting from the combination of green Tb<sup>3+</sup> and red Eu<sup>3+</sup> components, appear eventually.

As the Rietveld Refinement and DFT modeling reveal, the Tb<sup>3+</sup> and Eu<sup>3+</sup> ions tend to substitute the Al<sup>3+</sup> and Sr<sup>2+</sup> sites, respectively, which can result in the negative Sr vacancies (*i.e.*, V<sub>Sr</sub><sup>''</sup>) that can compensate the excess positive charge between Sr<sup>2+</sup> and Eu<sup>3+</sup>. In consequence, the defect complexes [Eu<sup>3+</sup><sub>Sr</sub> + V<sub>Sr</sub><sup>''</sup>], coming from the replacement type of Eu<sup>3+</sup> + Sr<sup>2+</sup> → Eu<sup>3+</sup><sub>Sr</sub> + V<sub>Sr</sub><sup>''</sup>, can form. This is also the underlying reason why Tb<sup>3+</sup> and Eu<sup>3+</sup> doped Sr<sub>3</sub>Al<sub>2</sub>O<sub>5</sub>Cl<sub>2</sub> phosphor can exhibit the afterglow luminescence. Although the afterglow luminescence is not the key point of this research subject, it, from the other side of view, reveals the possible existence of defects in the Tb<sup>3+</sup>, Eu<sup>3+</sup> doped Sr<sub>3</sub>Al<sub>2</sub>O<sub>5</sub>Cl<sub>2</sub> phosphor. Because of this, exciting at 376 nm can only lead to the anomalous Eu<sup>3+</sup> enhancement at earlier heating state. This can be ascribed to the discharge of electrons trapped in the defects, which is a little similar to the cases of LuVO<sub>4</sub>:Bi<sup>3+</sup> phosphor [43] and colloidal CdSe QDs [71-72]. No matter which the excitation wavelengths (*i.e.*, 376 nm, and 393 nm) have been used (**Figure 5(c-d)**), however, such anomalous PL phenomenon cannot

appear in the  $\text{Eu}^{3+}$  emission. The disappearance of  $\text{Tb}^{3+}$  emission excited at 393 nm indicates there is no energy transfer from  $\text{Eu}^{3+}$  to  $\text{Tb}^{3+}$ . The energy transfer from  $\text{Tb}^{3+}$  to  $\text{Eu}^{3+}$  is unidirectional. The  $\text{Tb}^{3+}$  luminescence at high temperature is dominated by the thermal quenching luminescence. Hence, we can conclude that the interplay of the temperature-induced accelerated energy transfer and release of electrons trapped by the crystal defects with trap depths of 78 °C and 129 °C is the reason for this temperature-induced anomalous  $\text{Eu}^{3+}$  related photoemission enhancement. Several previous works have shown the temperature-induced energy transfer [41, 66, 73] but significantly differ from the current PL observations that involve the temperature-dependent energy transfer interaction from one dopant (*i.e.*,  $\text{Tb}^{3+}$ ) that features a longer lifetime to another dopant (*i.e.*,  $\text{Eu}^{3+}$ ) that features a shorter lifetime.

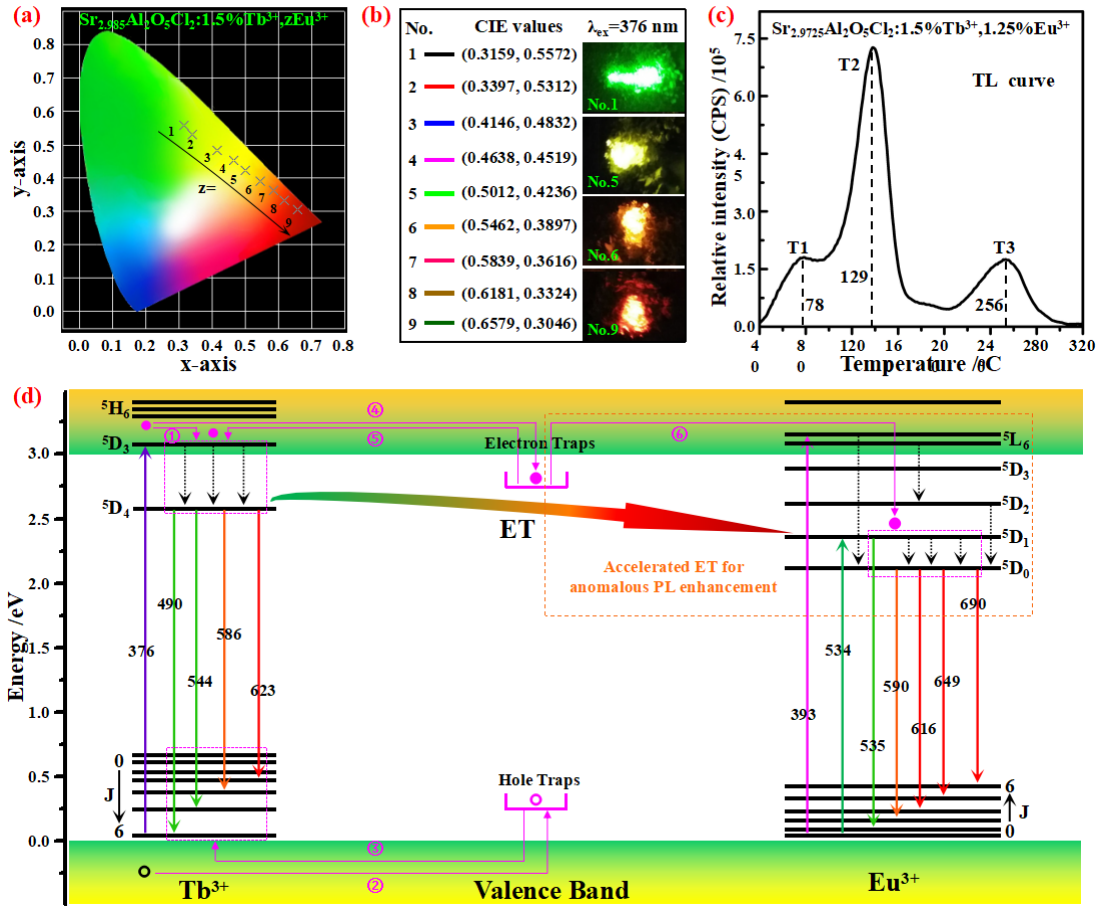


**Figure 7 (a)** CIE chromaticity coordinates of  $\text{Sr}_{2.985}\text{Al}_2\text{O}_5\text{Cl}_2:1.5\%\text{Tb}^{3+}, z\text{Eu}^{3+}$  ( $z = 0, 0.25\%, 0.5\%, 0.75\%, 1.0\%, 1.25\%, 1.5\%, 1.75\%, 2.0\%$ ) as calculated from the emission spectra of **Figure 2(d)**;

**(b)** The corresponding CIE values of the  $\text{Sr}_{2.985}\text{Al}_2\text{O}_5\text{Cl}_2:1.5\%\text{Tb}^{3+}, z\text{Eu}^{3+}$  samples; **(c)** TL glow curve of  $\text{Sr}_{2.9725}\text{Al}_2\text{O}_5\text{Cl}_2:1.5\%\text{Tb}^{3+}, 1.25\%\text{Eu}^{3+}$  sample; **(d)** Mechanistic profile for PL observation in the  $\text{Sr}_3\text{Al}_2\text{O}_5\text{Cl}_2:\text{Tb}^{3+}, \text{Eu}^{3+}$ . Noted that the depth of electron traps is 402 K, paths ①-⑥ denote the migration and recombination of the electron-hole pairs, and ET represents the energy transfer.

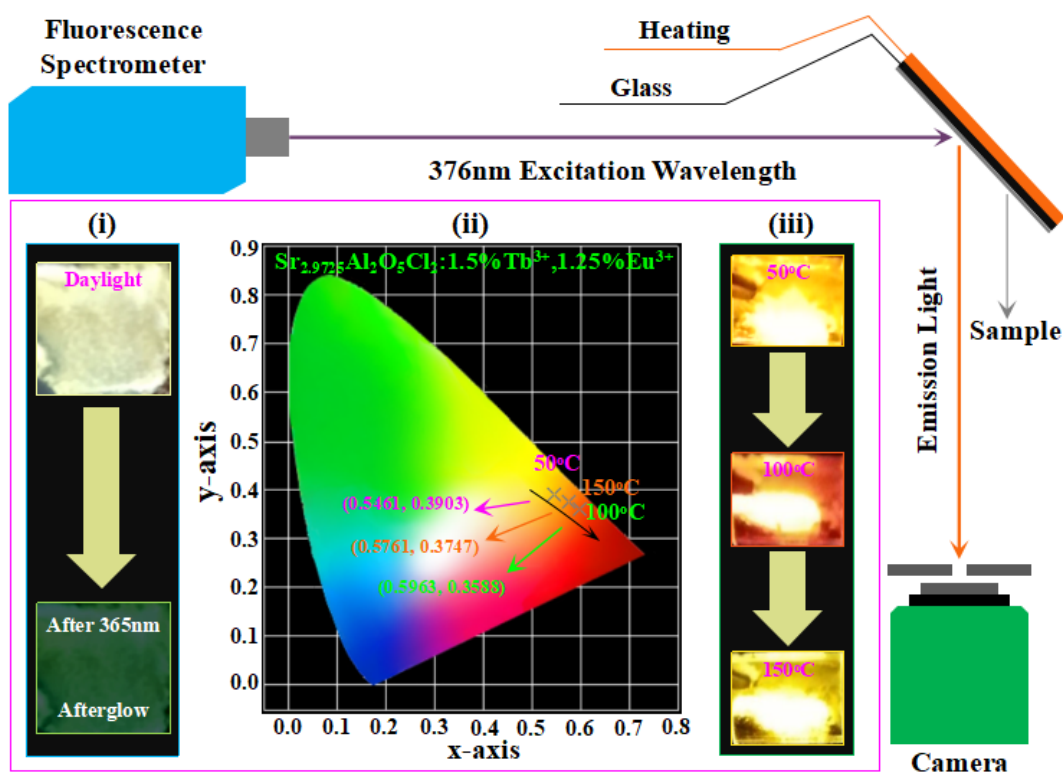


**Figure 8** A experimental setup consisted of the fluorescence spectrometer, heating instrument, and digital detection camera for recording the emission color. Inset is digital photographs of phosphor deposited glass taken under daylight and 365 nm excitation (i), and correlated typical CIE values (ii) and digital photographs (iii) upon excitation at 374 nm after heating at different temperatures.

### 3.7 Applications of targeted phosphor

According to a large number of previously-reported research or review articles, demo applications of luminescent phosphor materials in night-vision indicators, illumination (*e.g.*, wLEDs), displays and decorations *etc* have been reported extensively. In sharp contrast to these applications, on the basis of the PL characteristics of  $\text{Sr}_3\text{Al}_2\text{O}_5\text{Cl}_2:\text{Tb}^{3+}, \text{Eu}^{3+}$  phosphors, we would like to try some new applications. As a proof of concept, we first deposited the  $\text{Sr}_{2.9725}\text{Al}_2\text{O}_5\text{Cl}_2:1.5\%\text{Tb}^{3+}, 1.25\%\text{Eu}^{3+}$  powders on a piece of quartz glass (**Figure 8(i)**). Under the daylight, the faint yellow body of the sample can be observed. As we warmed this phosphor-deposited glass to the temperatures of 50 °C, 75 °C, 100 °C, 150 °C, and 200 °C, a sight variation of colors upon excitation at 376 nm can be observed. Since there is no heating device directly connected to the spectrometer, we first placed the quartz glass in a heating oven and then transferred it to a 376 nm UV beam that comes from the spectrometer. The five temperature points are the nominal temperatures that should be a bit lower than the practical temperature we used for taking the digital photos, but the collected time is

controlled to be less than 2 second. The simplified experimental setup for the emission color is given in **Figure 8**. After switching off a 365 nm UV lamp, the Tb<sup>3+</sup>-related greenish afterglow luminescence, which can last for dozens of minutes, appears (**Figure 8(i)**). This is different from the yellow color (**Figure 7(b)**). The temperature-induced anomalous Eu<sup>3+</sup>-related CIE values and related color changes are exhibited in the **Figure 8 (ii-iii)**. With such temporal color changes induced by temperature, the Sr<sub>3</sub>Al<sub>2</sub>O<sub>5</sub>Cl<sub>2</sub>:Tb<sup>3+</sup>,Eu<sup>3+</sup> phosphors upon with and without UV light feature the PL information encryption and decryption behavior, thus exhibiting great promising for anti-counterfeiting, temperature-controlled fluorescence sensor, and correlated data storage and security purpose.

#### 4. CONCLUSIONS AND OUTLOOK

In this work, we prepared and reported a type of Tb<sup>3+</sup>, Eu<sup>3+</sup> doped Sr<sub>3</sub>Al<sub>2</sub>O<sub>5</sub>Cl<sub>2</sub> phosphor, which enabled generating the tunable colors from green (0.3159, 0.5572) to red (0.6579, 0.3046) by controlling the doping ratios of Tb<sup>3+</sup> and Eu<sup>3+</sup> ions upon excitation at 376 nm. We confirmed the existence of the energy transfer from Tb<sup>3+</sup> to Eu<sup>3+</sup> ions and revealed it was happened via an electric dipole-quadrupole (*d-q*) interaction. On the basis of the time-resolved PL spectra, we further found the energy transfer from Tb<sup>3+</sup> to Eu<sup>3+</sup> in the Sr<sub>2.9725</sub>Al<sub>2</sub>O<sub>5</sub>Cl<sub>2</sub>:1.5%Tb<sup>3+</sup>,1.25%Eu<sup>3+</sup> sample begun at  $t = 5 \mu\text{s}$  and gradually ended  $t \geq 200 \mu\text{s}$ . More remarkable, we found the Sr<sub>3</sub>Al<sub>2</sub>O<sub>5</sub>Cl<sub>2</sub>:Tb<sup>3+</sup>,Eu<sup>3+</sup> phosphor not only held excellent resistance against thermal quenching but also featured the temperature-induced anomalous Eu<sup>3+</sup>-related emission enhancement at the earlier heating state. To unveil the reason, we employed the DFT calculations to screen all possibilities of crystal sites that could be substituted by Tb<sup>3+</sup> and Eu<sup>3+</sup> ions, and the results of which, together with the refined XRD information, allowed us to conclude the Eu<sup>3+</sup> and Tb<sup>3+</sup> tended to substitute for the Sr<sup>2+</sup> and Al<sup>3+</sup> sites, respectively. The TL glow curve revealed that the energy stored by the crystal defects generated by substitution of Sr<sup>2+</sup> with Eu<sup>3+</sup> could be released upon the thermal stimulation. Discussion on temperature-induced accelerated energy transfer and discharge of electrons trapped in defects with trap depths of 78 °C and 129 °C indicated that the interplay of both cases were the underlying reason for the temperature-induced Eu<sup>3+</sup>-related photoemission enhancement. We also presented the Sr<sub>3</sub>Al<sub>2</sub>O<sub>5</sub>Cl<sub>2</sub>:Tb<sup>3+</sup>,Eu<sup>3+</sup> phosphor featured the information encryption and decryption behavior, showing great promising for anti-counterfeiting, temperature-controlled fluorescence sensor, and correlated data storage and security purposes. Such applications are different from

most of previously-reported phosphor materials which are always suggested for night-vision indicators, illumination (*e.g.*, wLEDs), displays and decorations *etc.*

In addition to the results mentioned above, we had also measured the quantum efficiency (QE) for the  $\text{Sr}_{2.985}\text{Al}_2\text{O}_5\text{Cl}_2:1.5\%\text{Tb}^{3+}$ ,  $\text{Sr}_{2.99}\text{Al}_2\text{O}_5\text{Cl}_2:1.0\%\text{Eu}^{3+}$ , and  $\text{Sr}_{2.725}\text{Al}_2\text{O}_5\text{Cl}_2:1.5\%\text{Tb}^{3+}, 1.25\%\text{Eu}^{3+}$  samples, and they were 45%, 35% and 50%, respectively. Although these values were still not high when compared to the commercial green and red phosphors being used in the illumination, the point of this work, as we presented here, was not to focus on how to improve the luminescence efficiency, but to employ the well-shielded  $4f\text{Tb}^{3+}$  and  $\text{Eu}^{3+}$  ions as dual luminescent activators to realize the multicolor tuning in the  $\text{Sr}_3\text{Al}_2\text{O}_5\text{Cl}_2:\text{Tb}^{3+}, \text{Eu}^{3+}$  crystal host and reveal the dynamic energy transfer interaction between the two  $4f$  ions as well as to explore some hitherto unnoticed PL properties, typically at high temperature. Of course, in view of the temperature-triggered  $\text{Eu}^{3+}$  photoemission enhancement which is partly from the release of electrons trapped in the defects, our results could give researchers some new insights, *i.e.*, how to design new crystal materials and improve their PL properties by using the crystal defects that are always considered to have a bad impact on the PL properties. All in all, this work not only demonstrated the realization of tunable emission in the  $\text{Sr}_3\text{Al}_2\text{O}_5\text{Cl}_2$  host lattice by using the well-shielded  $4f\text{Tb}^{3+}$  and  $\text{Eu}^{3+}$  ions as dual luminescent centers, but also could provide new understanding on the energy transfer interaction between different dopants, paving some directive clues for researchers to study the energy transfer behavior behind the well-shielded  $4f$  ions and the substitution preferential problems in the crystal host lattices that have multi available sites in the future. Moreover, we expect the design concept can extend to discover more unnoticed PL properties in other crystal hosts that involve non-RE (*e.g.*,  $\text{Cr}^{3+}$ ,  $\text{Bi}^{3+}$ ,  $\text{Mn}^{2+}$ ,  $\text{Mn}^{4+}$ , *etc.*), other RE (*e.g.*,  $\text{Eu}^{2+}$ ,  $\text{Ce}^{3+}$ ,  $\text{Sm}^{3+}$ ,  $\text{Pr}^{3+}$ , *etc.*) ions or coupling arrangement of these ions, not limited to the  $\text{Sr}_3\text{Al}_2\text{O}_5\text{Cl}_2:\text{Tb}^{3+}, \text{Eu}^{3+}$  phosphor system.

#### **ACKNOWLEDGEMENT**

This work was jointly supported by the Innovation and Technology Commission of HKSAR through Hong Kong Branch of National Precious Metals Material Engineering Research Center, the City University of Hong Kong (Projects 9667143 and 7004902), and by NPRP grant No. 8-878-1-172 from the Qatar National Research Fund (A Member of the Qatar Foundation).

## REFERENCES

- [1] Ye, S.; Xiao, F.; Pan, Y. X.; Ma, Y. Y.; Zhang, Q. Y. Phosphors in phosphor-converted white light-emitting diodes: Recent advances in materials, techniques and properties. *Mater. Sci. Eng. R.* **2010**, *71*, 1-34.
- [2] Xia, Z. G.; Liu, Q. L. Progress in discovery and structural design of color conversion phosphors for LEDs. *Prog. Mater. Sci.* **2016**, *84*, 59-117.
- [3] Yin, H. B.; Chen, X. F.; Hou, R. J.; Zhu, H. J.; Li, S. Q.; Huo, Y. N.; Li, H. X. Ag/BiOBr Film in a Rotating-Disk Reactor Containing Long-Afterglow Phosphor for Round-the-Clock Photocatalysis. *ACS Appl. Mater. Interfaces* **2015**, *7*, 20076-20082.
- [4] Mei, Y. H.; Xu, H.; Zhang, J. C.; Ci, Z. P.; Duan, M. X.; Peng, S. L.; Zhang, Z. Y.; Tian, W.; Lu, Y.; Wang, Y. H. Design and spectral control of a novel ultraviolet emitting long lasting phosphor for assisting TiO<sub>2</sub> photocatalysis: Zn<sub>2</sub>SiO<sub>4</sub>:Ga<sup>3+</sup>, Bi<sup>3+</sup>. *J. Alloy. Compd.* **2015**, *622*, 908-912.
- [5] Liu, X. J.; Chu, H. P.; Li, J. L.; Niu, L. Y.; Li, C.; Li, H. L.; Pan, L. K.; Sun, C. Q. Light converting phosphor-based photocatalytic composites. *Catal. Sci. Technol.* **2015**, *5*, 4727-4740.
- [6] Yun, Y. J.; Kim, J. Y.; Choi, S. K.; Park, W. I.; Suh, J. Y.; Jung, H. K.; Kim, Y. S.; Choi, S. H. Dual spectra band emissive Eu<sup>2+</sup>/Mn<sup>2+</sup> co-activated alkaline earth phosphates for indoor plant growth novel phosphor converted-LEDs. *Phys. Chem. Chem. Phys.* **2017**, *19*, 11111-11119.
- [7] Deng, J. K.; Zhang, H. R.; Zhang, X. J.; Zheng, Y. J.; Yuan, J. Q.; Liu, H. Z.; Liu, Y. L.; Lei, B. F.; Qiu, J. B. Ultrastable red-emitting phosphor-in-glass for superior high-power artificial plant growth LEDs. *J. Mater. Chem. C* **2018**, *6*, 1738-1745.
- [8] Paul, L.; Dirk, V.; Peter, W. Storage Phosphors for Medical Imaging. *Materials* **2011**, *4*, 1034-1086.
- [9] Kaur, J.; Parganiha, Y.; Dubey, V.; Singh, D. A review report on medical imaging phosphors. *Res. Chem. Intermediat.* **2014**, *40*, 2837-2858.
- [10] Shang, M. M.; Li, C. X.; Lin, J. How to produce white light in a single-phase host. *Chem. Soc. Rev.*, **2014**, *43*, 1372-1386.
- [11] Kang, F. W.; Zhang, Y.; Peng, M. Y. Controlling the Energy Transfer via Multi Luminescent Centers to Achieve White Light/Tunable Emissions in a Single-Phased X2-Type Y<sub>2</sub>SiO<sub>5</sub>:Eu<sup>3+</sup>, Bi<sup>3+</sup> Phosphor For Ultraviolet Converted LEDs. *Inorg. Chem.* **2015**, *54*, 1462-1473.
- [12] Ogi, T.; Kaihatsu, Y.; Iskandar, F.; Wang, W. -N.; Okuyama, K. Facile Synthesis of New Full-Color-Emitting BCNO Phosphors with High Quantum Efficiency. *Adv. Mater.* **2008**, *20*, 3235-3238.

- [13] Huang, A. J.; Yang, Z. W.; Yu, C. Y.; Chai, Z. Z.; Qiu, J. B.; Xia, Z. G. Tunable and White Light Emission of a Single-Phased  $\text{Ba}_2\text{Y}(\text{BO}_3)_2\text{Cl}:\text{Bi}^{3+},\text{Eu}^{3+}$  Phosphor by Energy Transfer for Ultraviolet Converted White LEDs. *J. Phys. Chem. C* **2017**, *121*, 5267-5276.
- [14] Dai, P. P.; Zhang, X. T.; Bian, L. L.; Lu, S.; Liu, Y. C.; Wang, X. J. Color tuning of  $(\text{K}_{1-x},\text{Na}_x)\text{SrPO}_4:0.005\text{Eu}^{2+},\text{yTb}^{3+}$  blue-emitting phosphors via crystal field modulation and energy transfer. *J. Mater. Chem. C* **2013**, *1*, 4570-4576.
- [15] Li, G. G.; Geng, D. L.; Shang, M. M.; Zhang, Y.; Peng, C.; Cheng, Z. Y.; Lin, J. Color Tuning Luminescence of  $\text{Ce}^{3+}/\text{Mn}^{2+}/\text{Tb}^{3+}$ -Triactivated  $\text{Mg}_2\text{Y}_8(\text{SiO}_4)_6\text{O}_2$  via Energy Transfer: Potential Single-Phase White-Light-Emitting Phosphors. *J. Phys. Chem. C* **2011**, *115*, 21882-21892
- [16] Lü, W.; Hao, Z. D.; Zhang, X.; Luo, Y. S.; Wang, X. J.; Zhang, J. H. nable Full-Color Emitting  $\text{BaMg}_2\text{Al}_6\text{Si}_9\text{O}_{30}:\text{Eu}^{2+},\text{Tb}^{3+},\text{Mn}^{2+}$  Phosphors Based on Energy Transfer. *Inorg. Chem.* **2011**, *50*, 7846-7851.
- [17] Geng, D. L.; Shang, M. M.; Zhang, Y.; Lian, H. Z.; Lin, J. Color-Tunable and White Luminescence Properties via Energy Transfer in Single-Phase  $\text{KNaCa}_2(\text{PO}_4)_2:\text{A}$  ( $\text{A} = \text{Ce}^{3+}, \text{Eu}^{2+}, \text{Tb}^{3+}, \text{Mn}^{2+}, \text{Sm}^{3+}$ ) Phosphors. *Inorg. Chem.* **2013**, *52*, 13708-13718.
- [18] Kang, F. W.; Peng, M. Y.; Yang, X. B.; Dong, G. P.; Nie, G. C.; Liang, W. J.; Xu, S. H.; Qiu, J. R. Broadly tuning  $\text{Bi}^{3+}$  emission via crystal field modulation in solid solution compounds  $(\text{Y,Lu,Sc})\text{VO}_4:\text{Bi}$  for ultraviolet converted white LEDs. *J. Mater. Chem. C* **2014**, *2*, 6068-607.
- [19] Li, G. G.; Tian, Y.; Zhao, Y.; Lin, J. Recent progress in luminescence tuning of  $\text{Ce}^{3+}$  and  $\text{Eu}^{2+}$ -activated phosphors for pc-WLEDs. *Chem. Soc. Rev.* **2015**, *44*, 8688-8713.
- [20] Kang, F. W.; Zhang, H. S.; Wondraczek, L.; Yang, X. B.; Zhang, Y.; Lei, D. Y.; Peng, M. Y. Band-Gap Modulation in Single  $\text{Bi}^{3+}$ -Doped Yttrium-Scandium-Niobium Vanadates for Color Tuning over the Whole Visible Spectrum. *Chem. Mater.* **2016**, *28*, 2692-2703.
- [21] Tian, Y.; Wei, Y.; Zhao, Y.; Quan, Z. W.; Li, G. G.; Lin, J. Photoluminescence tuning of  $\text{Ca}_5(\text{PO}_4)_3\text{Cl}:\text{Ce}^{3+}/\text{Eu}^{2+},\text{Tb}^{3+}/\text{Mn}^{2+}$  phosphors: structure refinement, site occupancy, energy transfer and thermal stability. *J. Mater. Chem. C* **2016**, *4*, 1281-1294.
- [22] Li, X.; Wang, Z. J.; Liu, S. M.; Bao, Q.; Meng, X. Y.; Qiu, K. L.; Li, Y. B.; Li, Z. Q.; Yang, Z. P. Color-Tunable Luminescence Properties of  $\text{Bi}^{3+}$  in  $\text{Ca}_5(\text{BO}_3)_3\text{F}$  via Changing Site Occupation and Energy Transfer. *Chem. Mater.* **2017**, *29*, 8792-8803.
- [23] Xia, Z. G.; Liu, G. K.; Wen, J. G.; Mei, Z. G.; Balasubramanian, M.; Molochev, M. S.; Peng, L. C.; Gu, L.; Miller, D. J.; Liu, Q. L.; Poepelmeier, K. R. Tuning of Photoluminescence by Cation Nanosegregation in the  $(\text{CaMg})_x(\text{NaSc})_{1-x}\text{Si}_2\text{O}_6$  Solid Solution. *J. Am. Chem. Soc.* **2016**,

138, 1158-1161.

- [24] Xia, Z. G.; Ma, C. G.; Molokeev, M. S.; Liu, Q. L.; Rickert, K.; Poeppelmeier, K. R. Chemical Unit Cosubstitution and Tuning of Photoluminescence in the  $\text{Ca}_2(\text{Al}_{1-x}\text{Mg}_x)(\text{Al}_{1-x}\text{Si}_{1+x})\text{O}_7:\text{Eu}^{2+}$  Phosphor. *J. Am. Chem. Soc.* **2015**, *137*, 12494-12497.
- [25] Cao, B. Q.; Cai, W. P.; Zeng, H. B. Temperature-dependent shifts of three emission bands for ZnO nanoneedle arrays. *Appl. Phys. Lett.* **2006**, *88*, 161101.
- [26] Kang, F. W.; Peng, M. Y.; Lei, D. Y.; Zhang, Q. Y. Recoverable and Unrecoverable  $\text{Bi}^{3+}$ -Related Photoemissions Induced by Thermal Expansion and Contraction in  $\text{LuVO}_4:\text{Bi}^{3+}$  and  $\text{ScVO}_4:\text{Bi}^{3+}$  Compounds. *Chem. Mater.* **2016**, *28*, 7807-7815.
- [27] You, H. P.; Wang, Q. P.; Jin, Y. Temperature dependence of energy transfer in tunable white light-emitting phosphor  $\text{BaY}_2\text{Si}_3\text{O}_{10}:\text{Bi}^{3+}, \text{Eu}^{3+}$  for near UV LEDs. *J. Mater. Chem. C* **2015**, *3*, 11151-11162.
- [28] Zhang, M. F.; Liang, Y. J.; Tang, R.; Yu, D. Y.; Tong, M. H.; Wang, Q.; Zhu, Y. L.; Wu, X. Y.; Li, G. G. Highly efficient  $\text{Sr}_3\text{Y}_2(\text{Si}_3\text{O}_9)_2:\text{Ce}^{3+}, \text{Tb}^{3+}/\text{Mn}^{2+}/\text{Eu}^{2+}$  phosphors for white LEDs: structure refinement, color tuning and energy transfer. *RSC Adv.* **2014**, *4*, 40626-40637.
- [29] Chen, L.; Chen, K. J.; Hu, S. F.; Liu, R. S. Combinatorial chemistry approach to searching phosphors for white light-emitting diodes in  $(\text{Gd-Y-Bi-Eu})\text{VO}_4$  quaternary system. *J. Mater. Chem.* **2011**, *21*, 3677-3685.
- [30] Li, K.; Geng, D. L.; Shang, M. M.; Zhang, Y.; Lian, H. Z.; Lin, J. Color-Tunable Luminescence and Energy Transfer Properties of  $\text{Ca}_9\text{Mg}(\text{PO}_4)_6\text{F}_2:\text{Eu}^{2+}, \text{Mn}^{2+}$  Phosphors for UV-LEDs. *J. Phys. Chem. C* **2014**, *118*, 11026-11034.
- [31] Chen, R.; Hu, Y. H.; Chen, L.; Wang, X. J. Observation on a novel green-yellow afterglow in  $\text{Tb}^{3+}$  doped  $\text{Sr}_3\text{Al}_2\text{O}_5\text{Cl}_2$  phosphor. *Sci. Adv. Mater.* **2017**, *9*, 392-397.
- [32] Chen, W. B.; Wang, Y. H.; Zeng, W.; Han, S. C.; Li, G. Filling of trap and green long persistent luminescence in  $\text{Sr}_3\text{Al}_2\text{O}_5\text{Cl}_2:\text{Tb}^{3+}$ . *Opt. Mater.* **2014**, *36*, 1850-1854.
- [33] Song, Y. H.; Jia, G.; Yang, M.; Huang, Y. J.; You, H. P.; Zhang, H. J.  $\text{Sr}_3\text{Al}_2\text{O}_5\text{Cl}_2:\text{Ce}^{3+}, \text{Eu}^{2+}$ : A potential tunable yellow-to-white-emitting phosphor for ultraviolet light emitting diodes. *Appl. Phys. Lett.*, **2009**, *94*, 091902.
- [34] Ning, L.; Zhou, C.; Chen, W.; Huang, Y.; Duan, C.; Dorenbos, P.; Tao, Y.; Liang, H. Electronic Properties of  $\text{Ce}^{3+}$ -Doped  $\text{Sr}_3\text{Al}_2\text{O}_5\text{Cl}_2$ : A Combined Spectroscopic and Theoretical Study. *J. Phys. Chem. C* **2015**, *119*, 6785-6792.
- [35] Danuta, D.; Ronda, C.; Meijerink, A.; Jüstel, T. Red luminescence and persistent

- luminescence of  $\text{Sr}_3\text{Al}_2\text{O}_5\text{Cl}_2:\text{Eu}^{2+},\text{Dy}^{3+}$ . *J. Lumin.* **2013**, *141*, 150-154.
- [36] Chen, R.; Hu, Y. H. Luminescent properties of blue green  $\text{Sr}_3\text{Al}_2\text{O}_5\text{Cl}_2:\text{Pr}^{3+}$  and orange red  $\text{Sr}_3\text{Al}_2\text{O}_5\text{Cl}_2:\text{Eu}^{2+},\text{Pr}^{3+}$  afterglow phosphors. *Radiat. Meas.* **2015**, *80*, 38-45.
- [37] Liu, C.; Hou, D.; Yan, J.; Zhou, L.; Kuang, X.; Liang, H.; Huang, Y.; Zhang, B.; Tao, Y. Energy Transfer and Tunable Luminescence of  $\text{NaLa}(\text{PO}_3)_4:\text{Tb}^{3+}/\text{Eu}^{3+}$  under VUV and Low-Voltage Electron Beam Excitation. *J. Phys. Chem. C* **2014**, *118*, 3220-3229.
- [38] Zhang, X. G.; Zhou, L. Y.; Pang, Q.; Shi, J. X.; Gong, M. L. Tunable Luminescence and  $\text{Ce}^{3+} \rightarrow \text{Tb}^{3+} \rightarrow \text{Eu}^{3+}$  Energy Transfer of Broad band-Excited and Narrow Line Red Emitting  $\text{Y}_2\text{SiO}_5:\text{Ce}^{3+},\text{Tb}^{3+},\text{Eu}^{3+}$  Phosphor, *J. Phys. Chem. C* **2014**, *118*, 7591-7598.
- [39] Wang, C.; Zhou, T.; Jiang, J.; Geng, H.; Ning, Z.; Lai, X.; Bi, J.; Gao, D. Multicolor Tunable Luminescence Based on  $\text{Tb}^{3+}/\text{Eu}^{3+}$  Doping through a Facile Hydrothermal Route. *ACS Appl. Mater. Interfaces* **2017**, *9*, 26184-26190.
- [40] Sawada, K.; Nakamura, T.; Adachi, S. Abnormal photoluminescence phenomena in  $(\text{Tb}^{3+}, \text{Eu}^{3+})$  codoped  $\text{Ga}_2\text{O}_3$  phosphor, *J. Alloy. Compd.* **2017**, *678*, 448-455.
- [41] Kang, F. W.; Yang, X. B.; Peng, M. Y.; Wondraczek, L.; Ma, Z. J.; Zhang, Q. Y.; Qiu, J. R. Red Photoluminescence from  $\text{Bi}^{3+}$  and the Influence of the Oxygen Vacancy Perturbation in  $\text{ScVO}_4$ : A Combined Experimental and Theoretical Study. *J. Phys. Chem. C* **2014**, *118*, 7515-7522.
- [42] Wang, W. X.; Yang, P. P.; Cheng, Z. Y.; Hou, Z. Y.; Li, C. X.; Lin, J. Patterning of Red, Green, and Blue Luminescent Films Based on  $\text{CaWO}_4:\text{Eu}^{3+}$ ,  $\text{CaWO}_4:\text{Tb}^{3+}$ , and  $\text{CaWO}_4$  Phosphors via Microcontact Printing Route. *ACS Appl. Mater. Interfaces* **2011**, *3*, 3921-3928.
- [43] Kang, F. W.; Peng, M. Y.; Zhang, Q. Y.; Qiu, J. R. Abnormal Anti-Quenching and Controllable Multi-Transitions of  $\text{Bi}^{3+}$  Luminescence by Temperature in a Yellow-Emitting  $\text{LuVO}_4:\text{Bi}^{3+}$  Phosphor for UV-Converted White LEDs. *Chem. -Eur. J.* **2014**, *20*, 11522-11530.
- [44] Clark, S. J.; Segall, M. D.; Pickard, C. J.; Hasnip, P. J.; Probert, M. I. J.; Refson, K.; Payne, M. C. First principles methods using CASTEP. *Z. Krist. -Cryst. Mater.* **2005**, *220*, 567.
- [45] Perdew, J. P.; Burke, K.; Ernzerhof, M. Generalized Gradient Approximation Made Simple. *Phys. Rev. Lett.* **1996**, *77*, 3865.
- [46] Marzari, N.; Vanderbilt, D.; Payne, M. C. Ensemble Density-Functional Theory for *Ab Initio* Molecular Dynamics of Metals and Finite-Temperature Insulators. *Phys. Rev. Lett.* **1997**, *79*, 1337.
- [47] Probert, M. I. J.; Payne, M. C. *Phys. Rev. B* **2003**, *67*, 075204.
- [48] Huang, B. L.; Gillen, R.; Robertson, J. Study of  $\text{CeO}_2$  and Its Native Defects by Density

- Functional Theory with Repulsive Potential. *J. Phys. Chem. C* **2014**, *118*, 24248-24256.
- [49] Kleinman, L.; Bylander, D. M. Efficacious Form for Model Pseudopotentials. *Phys. Rev. Lett.* **1982**, *48*, 1425.
- [50] Louie, S. G.; Froyen, S.; Cohen, M. L. Nonlinear ionic pseudopotentials in spin-density-functional calculations. *Phys. Rev. B* **1982**, *26*, 1738.
- [54] Grinberg, I.; Ramer, N. J.; Rappe, A. M. Transferable relativistic Dirac-Slater pseudopotentials. *Phys. Rev. B* **2000**, *62*, 2311.
- [52] Rappe, A. M.; Rabe, K. M.; Kaxiras, E.; Joannopoulos, J. D. Erratum: Optimized pseudopotentials. *Phys. Rev. B* **1990**, *41*, 1227.
- [53] Huang, B. L. Native Point Defects in CaS: Focus on Intrinsic Defects and Rare Earth Ion Dopant Levels for Up-converted Persistent Luminescence. *Inorg. Chem.* **2015**, *54*, 11423.
- [54] Song, E. H.; Ding, S.; Wu, M.; Ye, S.; Xiao, F.; Zhou, S. F.; Zhang, Q. Y. Anomalous NIR Luminescence in Mn<sup>2+</sup>-Doped Fluoride Perovskite Nanocrystals. *Adv. Opt. Mater.* **2014**, *2*, 670-678.
- [55] Wen, H. L.; Zhu, H.; Chen, X.; Hung, T. F.; Wang, B. L.; Zhu, G. Y.; Yu, S. F.; Wang, F. Upconverting Near-Infrared Light through Energy Management in Core-Shell-Shell Nanoparticles. *Angew. Chem. Int. Ed.* **2013**, *52*, 13419-13423.
- [56] Deng, R. R.; Qin, F.; Chen, R. F.; Huang, W.; Hong, M. H.; Liu, X. G. Temporal full-colour tuning through non-steady-state upconversion. *Nat. Nanotechnol.* **2015**, *10*, 237-243.
- [57] Kang, F. W.; He, J. J.; Sun, T. Y.; Bao, Z. Y.; Wang, F.; Lei, D. Y. Plasmonic Dual-Enhancement and Precise Color Tuning of Gold Nanorod@SiO<sub>2</sub> Coupled Core-Shell-Shell Upconversion Nanocrystals. *Adv. Funct. Mater.* **2017**, 1701842.
- [58] Zhou, Y. H.; Lin, J.; Yu, M.; Wang, S. B.; Zhang, H. J. Synthesis-dependent luminescence properties of Y<sub>3</sub>Al<sub>5</sub>O<sub>12</sub>:Re<sup>3+</sup> (Re=Ce, Sm, Tb) phosphors. *Mater. Lett.* **2002**, *56*, 628-636.
- [59] Geng, D. L.; Shang, M. M.; Zhang, Y.; Cheng, Z. Y.; Lin, J. Tunable and White-Light Emission from Single-Phase Ca<sub>2</sub>YF<sub>4</sub>PO<sub>4</sub>:Eu<sup>2+</sup>,Mn<sup>2+</sup> Phosphors for Application in W-LEDs. *Eur. J. Inorg. Chem.* **2013**, 2947-2953.
- [60] Huang, C. H.; Wu, P. J.; Lee, J. F.; Chen, T. M. (Ca,Mg,Sr)<sub>9</sub>Y(PO<sub>4</sub>)<sub>7</sub>:Eu<sup>2+</sup>,Mn<sup>2+</sup>: Phosphors for white-light near-UV LEDs through crystal field tuning and energy transfer. *J. Mater. Chem.* **2011**, *21*, 10489-10495.
- [61] Xie, M. B.; Zhu, G. X.; Li, D. Y.; Pan, R. K.; Fu, X. H. Tunable white-light emission via energy transfer in single-phase LiGd(WO<sub>4</sub>)<sub>2</sub>:Re<sup>3+</sup> (Re = Tm, Tb, Dy, Eu) phosphors for

UV-excited WLEDs. *RSC Adv.* **2015**, *5*, 96272-96280.

[62] Kang, F. W.; Li, L. J.; Hang, J.; Lei, D. Y.; Peng, M. Y. Emission color tuning through manipulating the energy transfer from  $\text{VO}_4^{3-}$  to  $\text{Eu}^{3+}$  in single-phased  $\text{LuVO}_4:\text{Eu}^{3+}$  phosphors. *J. Mater. Chem. C*, **2017**, *5*, 390-398

[63] Peng, M. Y.; Wondraczek, L. Photoluminescence of  $\text{Sr}_2\text{P}_2\text{O}_7:\text{Bi}^{2+}$  as a red phosphor for additive light generation. *Opt. Lett.* **2010**, *35*, 2544-2546.

[64] Ma, M. X.; Zhu, D. C.; Zhao, C.; Han, T.; Cao, S. X.; Lei, Y.; Tu, M. J. Thermal degradation of  $\text{BaAl}_2\text{Si}_2\text{O}_8:\text{Eu}^{2+}$  phosphor excited by near ultraviolet light. *Chin. Sci. Bull.* **2012**, *14*, 1728-1732.

[65] Piao, X. Q.; Horikawa, T.; Hanzawa, H.; Machida, K. Characterization and luminescence properties of  $\text{Sr}_2\text{Si}_5\text{N}_8:\text{Eu}^{2+}$  phosphor for white light-emitting-diode illumination. *Appl. Phys. Lett.* **2006**, *88*, 161908.

[66] Dai, P. P.; Zhang, X. T.; Zhou, M.; Li, X. H.; Yang, J. K.; Sun, P. P.; Xu, C. S.; Liu, Y. C. Thermally Stable Pyrochlore  $\text{Y}_2\text{Ti}_2\text{O}_7:\text{Eu}^{3+}$  Orange-Red Emitting Phosphors. *J. Am. Ceram. Soc.* **2012**, *95*, 658-662.

[67] Zhang, X. M.; Yan, D. X.; Yuan, G. M.; Seo, H. J. Luminescent Properties of  $\text{Eu}^{3+}$ -Activated Fluorogermanate Based Red Phosphor with High Thermal Stability, *ECS Solid State Lett.* **2015**, *4*, R43-45.

[68] Qi, S. Y.; Xie, H. D.; Huang, Y. L.; II Kim, S.; Seo, H. J. A narrow red-emitting phosphor of  $\text{NaLa}_4[\text{Mo}_3\text{O}_{15}]\text{F}:\text{Eu}^{3+}$  with broad excitation band extending in blue wavelength region. *Opt. Mater. Express* **2014**, *4*, 190-197.

[69] Li, Y.; Gecevicius, M.; Qiu, J. R. Long persistent phosphors-from fundamentals to applications. *Chem. Soc. Rev.* **2016**, *45*, 2090-2136.

[70] Diana, C.; Rodríguez B.; Suchinder, K. S.; Pieter, D.; Bruno, V.; John, A. C. Persistent and Photostimulated Red Emission in  $\text{CaS}:\text{Eu}^{2+}$ ,  $\text{Dy}^{3+}$  Nanophosphors. *Adv. Opt. Mater.* **2015**, *3*, 551-557.

[71] Zhao, Y. M.; Riemersma, C.; Pietra, F.; Koole, R.; Donegá, C. de M.; Meijerink, A. High-Temperature Luminescence Quenching of Colloidal Quantum Dots. *ACS Nano* **2012**, *6*, 9058-9067.

[72] Wuister, S. F.; Houselt, A.; Donegá, C. de M.; Vanmaekelbergh, D.; Meijerink, A. Temperature Antiquenching of the Luminescence from Capped CdSe Quantum Dots. *Angew. Chem. Int. Ed.* **2004**, *43*, 3029-3033.